Monthly Notices of the ROYAL ASTRONOMICAL SOCIETY
MNRAS **523,** 6061–6081 (2023) https://doi.org/10.1093/mnras/stad1600
Advance Access publication 2023 June 6

Multiscale stellar associations across the star formation hierarchy in PHANGS–HST nearby galaxies: methodology and properties

Kirsten L. Larson,[1,2★] Janice C. Lee,[2,3] David A. Thilker,[4] Bradley C. Whitmore,[5] Sinan Deger,[2,6] James Lilly,[7] Rupali Chandar,[8] Daniel A. Dale,[7] Frank Bigiel,[9] Kathryn Grasha,[10] Brent Groves,[10,11] Stephen Hannon,[12] Ralf S. Klessen,[13,14] Kathryn Kreckel,[15] J. M. Diederik Kruijssen,[16] Adam K. Leroy,[17] Hsi-An Pan,[12] Erik Rosolowsky,[18] Eva Schinnerer,[12] Andreas Schruba,[19] Elizabeth J. Watkins[14] and Thomas G. Williams[12,20]

Affiliations are listed at the end of the paper

Accepted 2023 May 10. Received 2023 May 9; in original form 2022 November 7

ABSTRACT

We develop a method to identify and determine the physical properties of stellar associations using *Hubble Space Telescope* (*HST*) *NUV*−*U*−*B*−*V*−*I* imaging of nearby galaxies from the Physics at High Angular Resolution in Nearby GalaxieS with the *Hubble Space Telescope* (PHANGS–HST) survey. We apply a watershed algorithm to density maps constructed from point source catalogues Gaussian smoothed to multiple physical scales from 8 to 64 pc. We develop our method on two galaxies that span the distance range in the PHANGS–HST sample: NGC 3351 (10 Mpc) and NGC 1566 (18 Mpc). We test our algorithm with different parameters such as the choice of detection band for the point source catalogue (*NUV* or *V*), source density image filtering methods, and absolute magnitude limits. We characterize the properties of the resulting multiscale associations, including sizes, number of tracer stars, number of associations, and photometry, as well as ages, masses, and reddening from spectral energy distribution fitting. Our method successfully identifies structures that occupy loci in the *UBVI* colour–colour diagram consistent with previously published catalogues of clusters and associations. The median ages of the associations increase from log(age/yr) = 6.6 to log(age/yr) = 6.9 as the spatial scale increases from 8 to 64 pc for both galaxies. We find that the youngest stellar associations, with ages <3 Myr, indeed closely trace H II regions in H α imaging, and that older associations are increasingly anticorrelated with the H α emission. Owing to our new method, the PHANGS–HST multiscale associations provide a far more complete census of recent star formation activity than found with previous cluster and compact association catalogues.

Key words: galaxies: star clusters: general – galaxies: star formation.

1 INTRODUCTION

Star formation occurs over a large range in physical scales, from parsec-sized molecular clumps to large star-forming regions of a few hundred parsecs in the discs and nuclear regions of galaxies. Resolving star-forming regions and linking emission from young stars to the physical conditions and gas supply are critical to understanding the ubiquity of the Kennicutt–Schmidt relation (Schmidt 1959; Kennicutt 1998) and the variation of star formation efficiency across galaxies and galaxy types. To fully understand the star formation process, we need to connect the spatial distribution and time-scales of stars from their formation in molecular clouds to the destruction of their birth clouds and the removal of gas from feedback. The ultraviolet (UV)–optical imaging obtained for nearby galaxies by the Physics at High Angular Resolution in Nearby GalaxieS with the *Hubble Space Telescope* (PHANGS–HST) programme (Lee et al. 2022) will allow us to track the time-scales for star formation structure evolution from stars at parsec scales, to stellar populations on 100 pc scales, up to galactic scales.

The majority of star formation generally occurs in stellar associations (Lada & Lada 2003; Gouliermis 2018; Ward & Kruijssen 2018; Ward, Kruijssen & Rix 2020; Wright 2020, and references therein) with the compact star clusters forming at the densest peaks of this stellar hierarchy (Elmegreen 2008; Kruijssen 2012). Star clusters account for ∼1–50 per cent of the star formation in galaxies (Kruijssen 2012; Adamo et al. 2015, 2020; Johnson et al. 2016; Chandar et al. 2017; Krumholz, McKee & Bland-Hawthorn 2019; Krause et al. 2020). In order to get a more complete census of star formation in galaxies, we must therefore trace the more loosely bound stellar associations and larger hierarchical structures of star formation. The identification of stellar associations requires a different set of methods distinct from those used to produce single-peaked compact star cluster catalogues in order to segment the light distribution over a large range of physical scales. The refinement of such techniques is necessary to obtain a complete inventory of the youngest stellar populations and facilitate joint analysis of molecular clouds and H II regions.

★ E-mail: kilarson@stsci.edu

Previous studies of associations and star-forming regions have used a variety of methods to identify stellar associations and the larger hierarchical structures in nearby galaxies, including nearest neighbours (Gouliermis et al. 2010), the minimum spanning tree (e.g. Cartwright & Whitworth 2004; Bastian et al. 2007), two-point correlation functions (Elmegreen 2018), kernel density estimation (KDE) isopleths (Gouliermis et al. 2015, 2017), and most recently dendrograms (e.g. Rodríguez, Baume & Feinstein 2019; Larson et al. 2020). The nearest neighbours and two-point correlation functions provide good characterization of smaller stellar associations, while the minimum spanning tree is useful to quantify hierarchy and the degree to which structures are fractal in nature.

We desire to trace the structures at multiple physical scales in the hierarchy in a way that easily allows for comparisons between multiple galaxies and joint analysis of molecular clouds and H II regions. To achieve this goal, we combine techniques from both the kernel density estimation (Gouliermis et al. 2015, 2017) and dendrogram methods (e.g. Rosolowsky et al. 2008; Rodríguez et al. 2019; Larson et al. 2020). Both the kernel density method and dendrograms employ isodensity contours to quantify their hierarchy. Dendrograms identify the full branching tree of the hierarchy of any statistically significant branch in a more free-form fashion. This has its advantages of characterizing the multiscale structures and all corresponding peaks, or 'leaves', in the distribution by creating a new branch in the hierarchy every time a statistically significant structure is identified. However, the organic branching results in identified 'leaves' with a wide range of surface brightness cut-offs (see Rosolowsky et al. 2008, for more details) and makes it difficult to compare structures at common surface brightness levels. We have therefore chosen to develop a method that allows us to identify stellar associations and compute their hierarchical structure at distinct surface brightness cut-offs determined by physical size scales.

The kernel density method applied by Gouliermis et al. (2017) investigates the hierarchy of structures by grouping structures above surface brightness levels, while our new method groups structures by their physical size. By relying on a fixed ladder of physical scales, our method facilitates comparison between galaxies. This allows for investigations based on physical size scales since disc scale heights and fragmentation lengths can differ both between and within galaxies. The different levels of the stellar hierarchy can also be easily compared to ancillary data with a variety of resolutions while still preserving the connection to both smaller and larger structures in the hierarchy.

Our method uses a seeded watershed algorithm on local-background-filtered Gaussian kernel density maps of tracer stellar populations to systematically delineate stellar associations and hierarchical structures over a wide range of physical scales. Watershed algorithms have been widely applied for image segmentation in the broader field of computer vision. Pixel values in the image are treated as in a topographic map, and regions are defined by 'flooding' the images starting at user-defined marker positions until separate regions meet or until the boundaries reach a surface brightness equal to a specified value. The resulting regions identified by the watershed algorithm define our stellar associations at each level in the hierarchy.

Our methods have been developed to produce complete catalogues of stellar associations using the UV–optical imaging obtained by the PHANGS–HST survey (Lee et al. 2022). PHANGS–HST[1] is a component of the greater PHANGS[2] programme, which is building a comprehensive data base to enable multiphase, multiscale studies of the star formation process across the nearby spiral galaxy population. This effort consists of PHANGS–ALMA, an Atacama Large Millimeter/submillimeter Array (ALMA) CO(2–1) mapping programme covering a representative sample of 74 main-sequence galaxies (Leroy et al. 2021); PHANGS–MUSE, a Very Large Telescope (VLT) imaging programme of 19 of these galaxies with the MUSE optical Integral Field Unit (IFU) instrument (Emsellem et al. 2022); and PHANGS–HST, which has obtained $NUV-U-B-V-I$ imaging for the 38 galaxies from the PHANGS sample best suited for studies of resolved stellar populations (including all galaxies observed with MUSE).[3] Imaging with *JWST* in eight filters at 2–21 μm for the 19 galaxies with the full complement of ALMA, MUSE, and *HST* observations has been approved through the PHANGS–JWST Cycle 1 Treasury survey (Lee et al. 2022, PID: 2107). The ensemble of PHANGS observations yields an unprecedented data base of the observed and physical properties of ∼100 000 star clusters, associations, H II regions, and molecular clouds. With these basic units of star formation, PHANGS systematically charts the evolutionary cycling between gas and stars across a diversity of galactic environments found in nearby galaxies.

We focus the analysis on two galaxies, NGC 3351 and NGC 1566, to develop our methods. We choose these galaxies because they span the distance range of most of the galaxies in the PHANGS–HST sample (NGC 3351 is at 10 Mpc, while NGC 1566 is at 18 Mpc; Anand et al. 2021) and have been previously studied by the LEGUS programme (Calzetti et al. 2015) to allow for catalogue comparisons. The two galaxies exhibit different morphologies and global properties, and provide a test of our method over a large range of galactic environments and dynamical structures, including bars, spiral arms, and star-forming rings. LEGUS star cluster catalogues have also been publicly released for both galaxies (Adamo et al. 2017), which enables comparison of the stellar associations found here to compact associations and star clusters that have been identified and studied using independent methods. LEGUS has also analysed the distribution of star formation in NGC 1566 in a hierarchical manner using KDE isopleths (Gouliermis et al. 2017).

This paper is part of a series that presents the major components of the overall PHANGS–HST data products: overview of survey design, pipeline, and data products (Lee et al. 2022); source detection and selection of compact star cluster candidates (Thilker et al. 2022); aperture correction and quantitative morphologies of star clusters (Deger et al. 2022); star cluster candidate classification (Whitmore et al. 2021); deep learning for neural network classification of star clusters (Wei et al. 2020); stellar association identification and analysis (this paper); spectral energy distribution (SED) fitting with CIGALE: *Code Investigating GALaxy Emission*[4] (Boquien et al. 2019; Turner et al. 2021); and constraints on galaxy distances through analysis of the Tip of the Red Giant Branch (TRGB) as observed in the PHANGS–HST parallel pointings (Anand et al. 2021).

This paper is organized as follows. We begin in Section 2 by describing the *HST* data used in this analysis. In Section 3, we describe our method for identifying stellar associations. We describe our process for selecting tracer stars that are used to observationally delineate stellar associations, the creation of filtered Gaussian kernel density maps, the watershed algorithm used to define the

[1] https://phangs.stsci.edu/
[2] http://www.phangs.org

[3] Galaxies are selected to be relatively face-on, avoid the Galactic plane, and have robust molecular cloud populations to facilitate joint analysis of stellar populations and molecular clouds (Lee et al. 2022).
[4] https://cigale.lam.fr

Table 1. Galaxy properties.

Name	RA (deg)	Dec. (deg)	Distance (Mpc)	Stellar mass ($M_\odot$)	SFR ($M_\odot$ yr^{-1})	Morph
NGC 3351	160.99065	11.70367	10	1.88e10 (0.10 dex)	1.2 (0.2)	Sb
NGC 1566	65.00159	−54.93801	18	4.56e10 (0.10 dex)	4.4 (0.2)	SABb

Note. Properties of NGC 3351 and NGC 1566.

regions bounding the associations, and the parameters involved in the definition process. In Section 4, we describe our strategy for measuring photometry within the multiscale associations, and for inferring ages, masses, and reddenings of the stellar associations via SED fitting using the CIGALE package.

We present the results of this methodology in Section 5 by characterizing the observed and physical properties of the ensemble population of stellar associations. We compare our sample with the star clusters and compact associations identified by the LEGUS programme, and discuss their relationship with both H α observations and molecular clouds identified by the PHANGS–ALMA survey. Finally, we conclude by summarizing the key findings of our analysis in Section 8, and discuss future work. The method presented here will be applied to the full sample of 38 PHANGS–HST galaxies to produce multiscale association catalogues to be publicly released together with the scripts used.

2 SAMPLE AND DATA

NGC 3351 is an Sb spiral galaxy with a mass of 1.88×10^{10} $M_\odot$ and a star formation rate (SFR) of 1.165 $M_\odot$ yr^{-1} (Leroy et al. 2021). It has both an inner and outer star-forming ring connected by a weak bar structure. NGC 1566 is an SABb spiral galaxy with a weak bar, two prominent star-forming spiral arms, and is ∼4 times more massive than NGC 3351. These basic properties and references are summarized in Table 1.

As described in the PHANGS–HST survey paper (Lee et al. 2022), all galaxies in the PHANGS–HST programme have *HST F275W* (NUV), *F336W* (*U*), *F438W* (*B*), *F555W* (*V*), and *F814W* (*I*) imaging with Wide Field Camera 3 (WFC3) or Advanced Camera for Surveys (ACS), as well as CO(2–1) observations with ALMA. For NGC 3351, two *HST* fields with imaging in these five bands are available, one obtained by LEGUS (Calzetti et al. 2015, PID 13364) in 2014, and another for the PHANGS–HST programme in 2019 (Lee et al. 2022, PID 15654). As discussed in Lee et al. (2022) and Turner et al. (2021), while the LEGUS observation strategy was to maximize radial coverage outward from the nucleus, PHANGS–HST aims to maximize the *HST* coverage with the available PHANGS–ALMA CO mapping, which resulted in overlapping but complementary observations for NGC 3351. NGC 1566 was observed by LEGUS in 2013. No additional *HST* observations were taken by PHANGS–HST since the available observations provided sufficient coverage of the ALMA CO map. Fig. 1 shows the footprints of the *HST* imaging together with those for the MUSE and ALMA CO maps, overlaid on Digitized Sky Survey images.[5] Exposure times are given in Table 2.

Our analysis makes use of DOLPHOT source catalogues, which are produced as the first step in the overall PHANGS–HST catalogue pipeline (Lee et al. 2022). These DOLPHOT catalogues are used as the base for both the PHANGS–HST cluster detection pipeline (Thilker et al. 2022) and the hierarchical stellar structure pipeline presented in this paper. The DOLPHOT photometry package (v2.0; Dolphin 2002) uses point spread function (PSF)-fitting to detect and deblend sources in the high-resolution *HST* images. The DOLPHOT source catalogue provides PSF-fitted photometry in all available bands as well as characteristics of the source (sharpness, roundness, chi-square, signal-to-noise ratio, crowding, and quality flag) for every detection. The DOLPHOT source characteristics are used to perform quality cuts on the sample as described in Section 3.1 to select the point sources used to trace the stellar associations. Thilker et al. (2022) provide a detailed description of the production of DOLPHOT catalogues for PHANGS–HST and list the adopted DOLPHOT parameters.

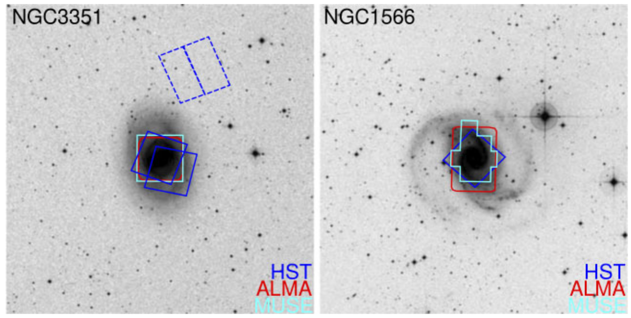

Figure 1. Footprints of the *HST* (blue), ALMA (red), and MUSE (cyan) coverage for NGC 3351 and NGC 1566. The PHANGS–HST imaging for NGC 3351 also included ACS *V*- and *I*-band parallel observations (footprint shown as dotted blue box) to enable distance measurements (Anand et al. 2021).

3 MULTISCALE STELLAR ASSOCIATION IDENTIFICATION METHOD

3.1 Selection of tracer stars

The first step is to select point sources from the DOLPHOT source catalogues to serve as 'tracer' stars, the positions of which, with appropriate selection, reveal the hierarchical structure of multiscale stellar associations.

We perform our analysis using both *NUV*- and *V*-band light as the detection band for the DOLPHOT stellar catalogues. The *NUV*-band light preferentially traces the youngest stellar populations, which is critical for comparison with molecular clouds. The *V*-band light facilitates comparisons to compact star cluster catalogues from both PHANGS–HST and LEGUS, which are *V*-band selected (Adamo et al. 2017; Lee et al. 2022; Thilker et al. 2022).

For the selection of tracer stars in the *NUV*-band,we use the following criteria:

(i) *NUV*-band signal-to-noise >7,

[5]The Digitized Sky Surveys were produced at the Space Telescope Science Institute under US Government grant NAG W-2166. The images are based on photographic data obtained using the Oschin Schmidt Telescope on Palomar Mountain and the UK Schmidt Telescope. The plates were processed into the present compressed digital form with the permission of these institutions.

Table 2. *HST* exposure times.

Name	*F275W* (s)	*F336W* (s)	*F438W* (s)	*F555W* (s)	*F814W* (s)	PID
NGC 3351-N	2190	1110	1050	670	830	15 654
NGC 3351-S	2361	1062	908	1062	908	13 364
NGC 1566	2382	1119	965	1143	989	13 364

Note. HST WFC3/UVIS imaging exposure times for NGC 3351 and NGC 1566. Data for NGC 1566 are from the LEGUS programme while new data for NGC 3351 were obtained by PHANGS–HST.

(ii) *NUV*-band sharpness[2] < 0.15,
(iii) *NUV*-band quality flag <4,
(iv) *U*-band signal-to-noise >3.

The sharpness criterion preferentially selects unresolved point sources. A perfectly fitted star has a sharpness of zero and a well-fitted star in an uncrowded field has a sharpness value between −0.3 and 0.3 (Dolphin 2002). We chose a more relaxed cut-off sharpness[2] < 0.15 to allow for effects from crowding. The DOLPHOT quality flag criterion ensures that we only consider unsaturated sources with well-determined photometry. A corresponding minimum detection in the *U*-band helps remove artefacts.

Similarly, the criteria for the tracer star selection in the *V*-band are:

(i) *V*-band signal-to-noise >7,
(ii) *V*-band sharpness[2] < 0.15,
(iii) *V*-band quality flag <4,
(iv) *B*-band signal-to-noise >3,
(v) (*V*-band flux/*V*-band sky level) ≥2.0.

Since the *V*-band data have more diffuse background emission, the *V*-band selection has an additional criterion to remove objects with high local sky background. This ensures that DOLPHOT sources included as tracer stars have significant detections above their local galactic environment. Additionally, foreground galactic stars are masked out and excluded from the tracer stars for both NUV- and *V*-band selection.

Our selection criteria result in magnitude limits of *NUV* <25.4 and *V* <27.2 mag for NGC 3351, which correspond to absolute magnitudes of $M_{\rm NUV} < -4.7$ and $M_{\rm V} < -2.8$ for a distance of 10 Mpc. Likewise, for the more distant NGC 1566 at 18 Mpc, these limits are *NUV* <24.9 and *V* <27.0 mag, and $M_{\rm NUV} < -6.3$ and $M_{\rm V} < -4.2$. The effects that the different absolute magnitude cuts have on the final results are explored in Section 5.5. We find that the different absolute magnitude limits do not affect the size or age distributions of the resulting associations but do result in fewer associations and a slight increase of the average log(M/M$_{\odot}$) by ∼0.2 dex. Since the overall change in the determined parameters is small, we chose to keep with a simple signal-to-noise selection and not apply an absolute magnitude cut on tracer stars to allow for a more complete comparison to the cluster catalogues (Adamo et al. 2017; Thilker et al. 2022) and data from other telescopes.

While our criteria for the tracer stars are designed to select point-like sources, they do not guarantee that all sources are in fact individual stars. Fig. 2 shows a *UBVI* diagram of the *V*-band selected tracer stars as a purple density grid compared to both the Padova stellar model tracks[6] (grey points, Girardi et al. 2002; Marigo et al. 2008) and the solar metallicity single-aged stellar population (SSP) models from Bruzual & Charlot (2003) (BC03, red line). Most of the tracer stars lie redward of the Padova stellar tracks. Some tracers, shown as purple stars, lie beyond the Humphrys–Davidson limit of $M_{\rm V} < -10$ mag and are therefore too bright to be individual stars. Since the goal is to find stellar associations, it is acceptable for our purposes if some of the tracer objects are in fact double stars or even unresolved clusters. The position of LEGUS identified Class 1, 2, and 3 objects are also shown as red, green, and blue points for comparison. LEGUS Class 1 and Class 2 objects are identified as compact star clusters while Class 3 objects are multipeaked compact associations. The LEGUS objects should be well-characterized by an SSP model and lie along and to the right of the BC03 SSP track.

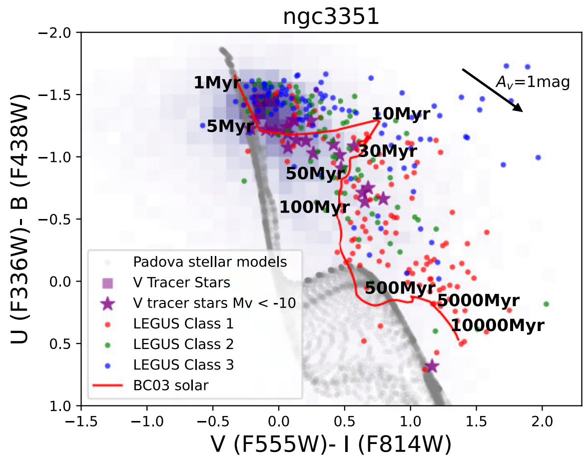

Figure 2. *UBVI* colour–colour diagram of the *V*-band tracer stars for NGC 3351. Grey points show the position of the Padova stellar models and the red line traces the path of a solar metallicity, single-aged stellar population from BC03. LEGUS objects are shown as red (Class 1 clusters), green (Class 2 clusters), and blue (Class 3 compact associations) points and tracer stars with $M_{\rm V} < -10$ mag are shown as purple stars.

3.2 Tracer star density maps

Once the tracer stars are identified, they are used to create a simplified map on which we can use the watershed algorithm to identify stellar associations. The steps to develop the tracer star density maps that will undergo segmentation are as follows.

A position map of the tracer stars' positions is created with the same shape and scale as the *HST* image. The position map has a value of one at the pixel position of the tracer stars and a value of zero at all other pixels. The location of *NUV* tracer stars is shown for regions in NGC 3351 and NGC 1566 in Figs 3(C) and 4(C). Gaussian kernel density maps are then created by smoothing the position map with a Gaussian profile with different full width at half-maximum (FWHM): 8, 16, 32, 64, 128, and 256 pc, where each successive smoothing level is two times as large as the preceding level, and

[6] http://stev.oapd.inaf.it/cgi-bin/cmd

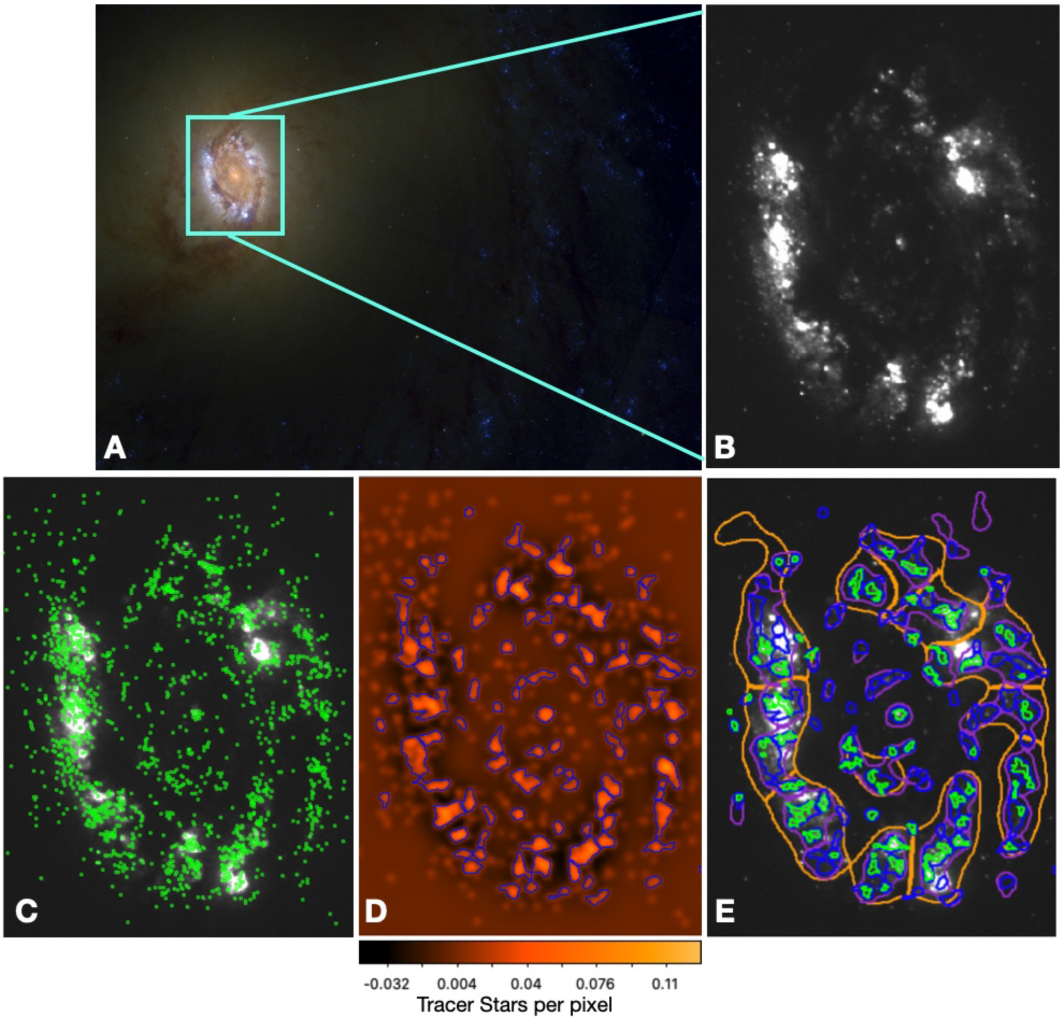

Figure 3. An illustration of our watershed procedure for identifying stellar associations over multiple scales. *(Panel A)* An *HST* three-colour image of NGC 3351 (Red: WFC3/UVIS *F*814*W*, Green: WFC3/UVIS *F*555*W*, Blue: WFC3/UVIS *F*438*W* + *F*336*W* + *F*275*W*). *(Panel B)* The *NUV* image of the centre of NGC 3351. *(Panel C)* The *NUV* image of the centre of NGC 3351 with the position of all *NUV* tracer stars shown as green points. *(Panel D)* The 16-pc filtered *NUV* tracer star density map for the centre of NGC 3351. The image is in units of tracer stars per pixel. The cut-off threshold is set to 1 FWHM and the 16-pc watershed regions are shown in blue. *(Panel E) NUV* image of the centre of NGC 3351 with 8, 16, 32, and 64-pc levels overplotted as corresponding green, blue, purple, and orange regions. At 0.0396 arcsec pixel^{-1}, one WFC3 pixel maps to 1.9 pc pixel^{-1} at a distance of 10 Mpc for NGC 3351.

where the two largest smoothing levels are used to construct a high-pass filter as described below. Each resulting Gaussian profile in the smoothed map, regardless of the size, will have a total value of 1 resulting in a smoothed number surface density map. The different smoothing levels allow us to trace the hierarchical structure at different physical scales. A lower limit in the smoothing level is set for each galaxy dependent on the galaxy's distance: 8 pc for NGC 3351 and 16 pc for NGC 1566. The smallest smoothing scales of 8 and 16 pc are chosen to approximately match the aperture size of 4 pixels (in radius) that is used for stellar cluster identification at the galaxies' distances given the resolution of WFC3 of 0.0396 arcsec pixel^{-1} (Adamo et al. 2017; Lee et al. 2022; Thilker et al. 2022). The smallest smoothing levels will therefore enable identification and comparison of stellar associations that overlap in size with objects in compact cluster catalogues. These smoothed tracer star density maps are then processed using a high-pass filter to emphasize the detailed structure at the chosen smoothing scale. The high-pass filter is applied by subtracting a tracer star density map that is smoothed with a larger Gaussian kernel. For example, the filtered 16-pc tracer star density map, as shown in Figs 3(D) and 4(D), is created by subtracting a map which is smoothed to 64 pc (a scale 4 times larger). The high-pass filter acts as a local background subtraction, filtering out the underlying distribution of stars in the image and emphasizing the structure at each smoothing scale. These smoothed, high-pass filtered tracer star density maps are then segmented using the watershed algorithm, as shown in Figs 3 (E) and 4 (E) and described in Section 3.3, to define stellar associations at different scales. In Appendix A, we compare the use of two different high-pass filters and select the 4 times high-pass filter for our sample as this filter step produces a tighter distribution of region sizes at all smoothing scales.

3.3 Watershed parameters

We use the seeded watershed routine from the publicly available PYTHON package SCIKIT-IMAGE (SKIMAGE.SEGMENTATION.WATERSHED) to define our stellar associations. We choose this particular watershed routine since it allows the user

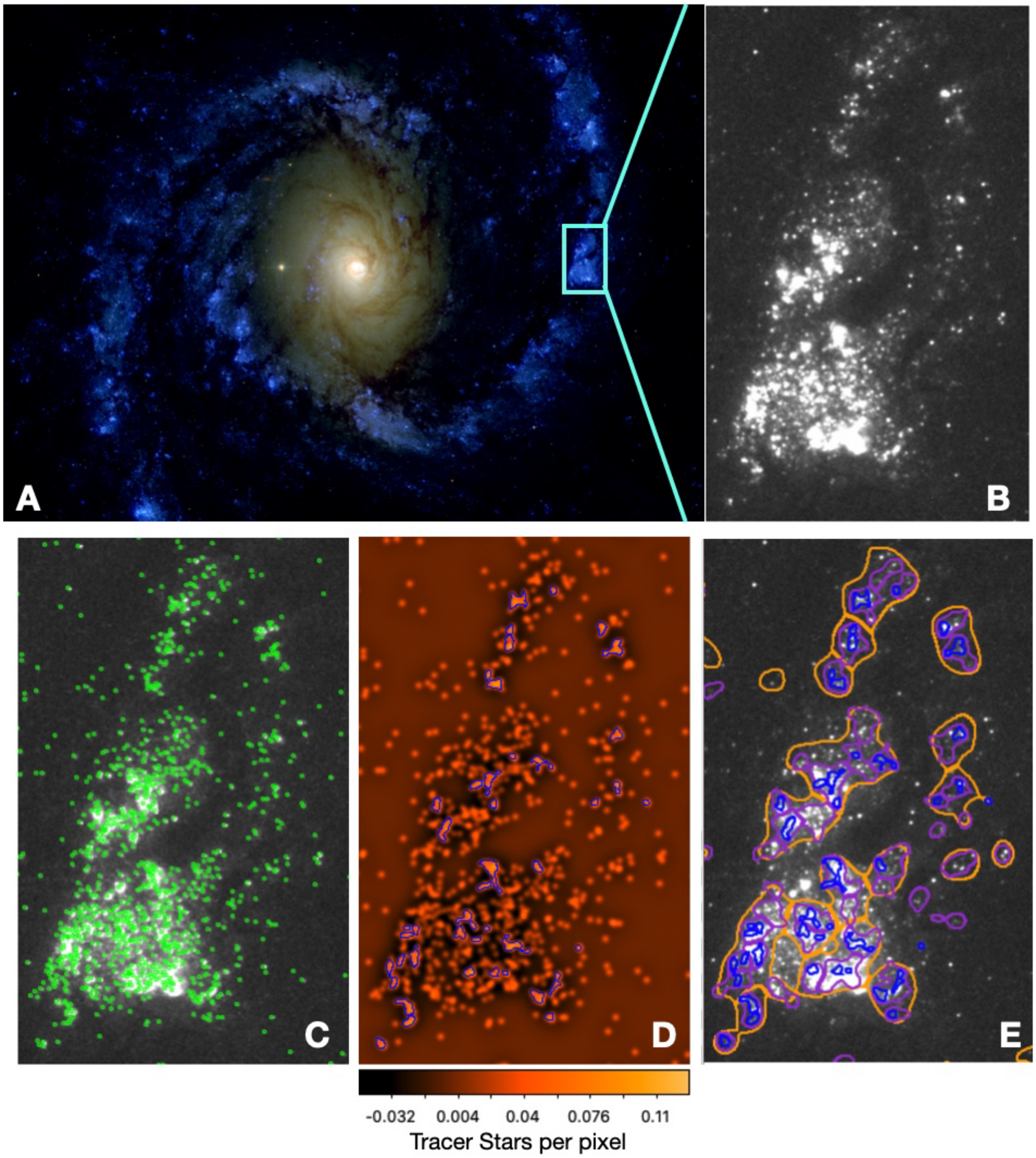

Figure 4. Same as Fig. 3, except for NGC 1566. At 0.0396 arcsec pixel^{-1}, one WFC3 pixel maps to 3.5 pc pixel^{-1} at a distance of 18 Mpc for NGC 1566. *(Panel A)* The *HST* three-colour image for NGC 1566 (Red: WFC3/UVIS *F*814*W*, Green: WFC3/UVIS *F*555*W*, Blue: WFC3/UVIS *F*438*W* + *F*336*W* + *F*275*W*). *(Panel B)* For illustration, we show a zoom-in of the *NUV* image on a portion of the spiral arm with a bright star-forming region in NGC 1566. *(Panel C)* The *NUV* image of the star-forming region in NGC 1566 with the position of all *NUV* tracer stars shown as green points. *(Panel D)* The 16-pc filtered *NUV* tracer star density map for the zoom in region of NGC 1566. The image is in units of tracer stars per pixel. The cut-off threshold is set to 1 FWHM and the 16-pc watershed regions are shown in blue. *(Panel E) NUV* image of NGC 1566 with 16, 32, and 64-pc levels overplotted as corresponding blue, purple, and orange regions. Star clusters are intentionally not included as tracer stars and therefore may not be included in the stellar association regions.

to control both the identification of the marker positions, which serve as the starting points from which regions are 'flooded' or grown, as well as to provide an image mask for pixels to consider when creating the segmented regions.

We develop a procedure to determine the marker positions and to produce the image mask using two free parameters:

(i) Peak threshold: the level above which marker positions are identified.

(ii) Edge threshold: the level above which image mask pixels are valid (have value of 1).

We tie the values of both parameters to the characteristics of a single object on the smoothed, filtered tracer star density maps. We define the peak threshold to be 1.5 times the maximum value for a single object to ensure that there will be at least two point-like sources per region. We use an edge threshold equal to the surface 'brightness' at the FWHM of a single object. Both of these values vary as a function of: (i) the distance of the galaxy, since the FWHM of the Gaussian kernels used to smooth the images are defined in parsecs, and (ii) the smoothing level itself.

We define our marker positions as the local maxima of the smoothed, filtered tracer star density map using the routine SKIMAGE.FEATURE.PEAK_LOCAL_MAX. The local maxima function re-

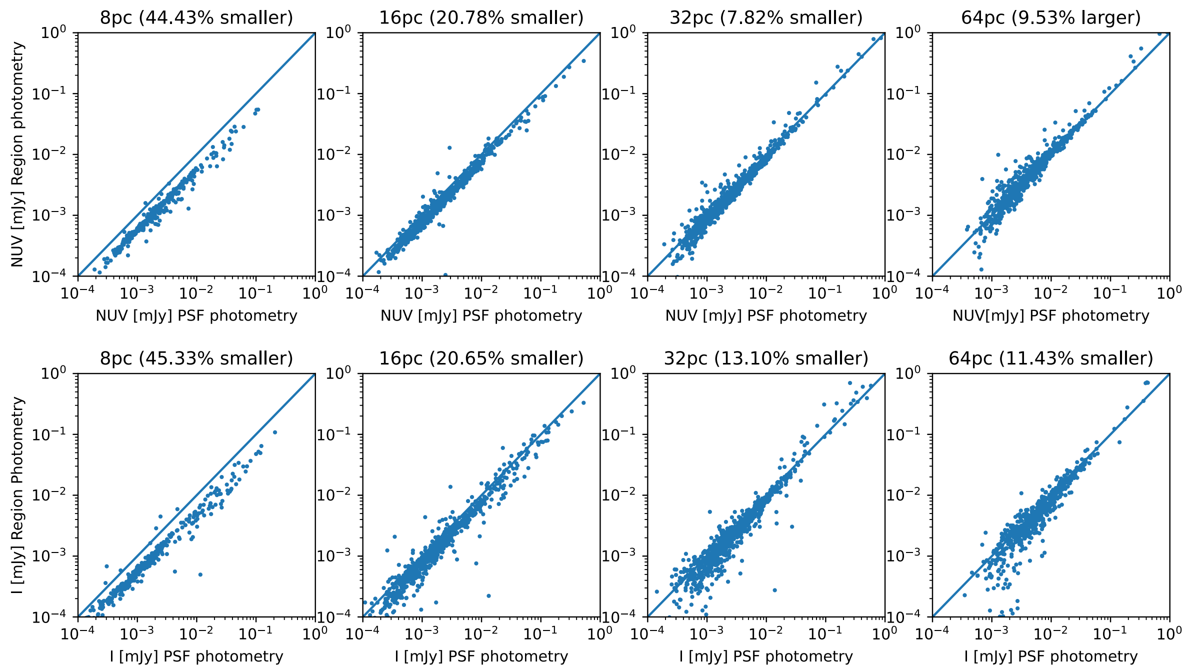

Figure 5. Comparison of regional and PSF photometry of stellar association for NGC 3351 for all scales (8–64 pc). Top row shows the comparison of *NUV*-band photometry and bottom row shows the comparison for *V*-band photometry. The title of each sub-figure states the average difference between the regional and PSF photometry.

quires both a minimum distance and threshold value to define the local maxima. We set the minimum allowed distance between maxima equal to the FWHM of a single object.

4 PHOTOMETRY AND SED FITTING METHODS

4.1 Stellar association photometry

In this section, we describe how we perform the photometry in the stellar associations which we use for the determination of physical properties. All light from within the bounds of an association is used in the photometry for that structure. The measured photometry stated is always the total flux of the region. Therefore, photometry for larger scale associations include light from any contained smaller scale associations. Since the stellar associations are often irregular in shape and by definition contain multiple stellar PSFs, we cannot assume that the standard aperture correction calculated for the compact cluster catalogues is appropriate for these regions (Deger et al. 2022). We therefore perform both regional pixel photometry and PSF photometry to test which procedure best recovers the total flux of the associations at all scale levels.

We first measure the flux of the stellar associations using standard regional pixel photometry. Regional photometry is performed by measuring the flux inside the stellar association regions and calculating the local background from an annulus around the region. Flux from all pixels within the regions are included in the photometry, therefore flux from compact clusters and diffuse emission within the aperture will also add to the regional photometry. We then measure PSF photometry of the stellar associations using DOLPHOT identified sources.

The PSF photometry of the stellar associations is found by summing DOLPHOT PSF photometry from all the DOLPHOT sources contained within the region. The photometric error for the associations is calculated by propagating the DOLPHOT photometry errors for the individual sources. While the definition of the associations only uses DOLPHOT sources that pass the tracer star selection (see Section 3.1), the PSF photometry uses all DOLPHOT sources. Bright foreground stars are masked out from the tracer stars and are excluded from the association regions. Therefore, the total number of DOLPHOT sources contained within an association and used for photometry can be greater than the number of selected tracer stars used to define the associations. We discuss this later in Section 5.2. No additional selection criteria are applied to the DOLPHOT sources. DOLPHOT only fits sources above the background with PSF-fitted photometry, therefore no additional background subtraction is required for the PSF photometry.

DOLPHOT is iteratively fitted 5 times. The highest signal-to-noise sources are fitted in the first pass, while the subsequent passes allow for fainter sources to be fitted in the residuals. Not all DOLPHOT sources are point sources, but the inclusion of all DOLPHOT sources in the photometry allows for the total flux of the region to be recovered. Since the same initial DOLPHOT catalogue is used for both the stellar association pipeline and the single-peaked compact cluster pipeline, it is possible for compact clusters to be included as part of a larger stellar association. As we will show in Sections 5.3 and 5.4, the observed and physical properties appear to be reasonable (e.g. the colours of the associations track that of a single-aged stellar population) and sufficient for this proof of concept demonstration.

We compare the regional sky subtracted pixel photometry to the PSF photometry of the stellar associations. Fig. 5 shows how both the *NUV*- and *V*-band regional and PSF photometry compare for NGC 3351. On average, the regional photometry is less than the PSF photometry. The difference is largest at the 8-pc scale level with the regional photometry being on average 45-per cent smaller than the PSF photometry. The difference decreases as the regions get larger

Table 3. NGC 3351 region properties.

Scale level (pc)	(pix)	(arcsec)	nRegions	Radius med (.25Q,.75Q) (pc)	nTracer med (.25Q,.75Q)	nDOLPHOT med (.25Q,.75Q)	M_V (mag) med (.25Q,.75Q)
NGC 3351 *NUV*-band tracer stars							
8	4.16	0.165	334	6.23 (5.53,7.66)	3 (3,6)	4 (3,6)	−6.8 (−7.88,−6.01)
16	8.33	0.33	807	12.4 (10.3,15.3)	4 (3,7)	7 (4,11)	−6.86 (−7.8,−6.1)
32	16.7	0.66	838	26.1 (21.6,32.4)	5 (3,8)	16 (10,26)	−7.06 (−7.97,−6.35)
64	33.3	1.32	641	55.2 (45.2,67.4)	7 (4,13)	49 (29,74)	−7.71 (−8.47,−7.03)
NGC 3351 *V*-band tracer stars							
8	4.16	0.165	557	6.03 (5.31,7.11)	3 (2,5)	4 (3,5)	−6.16 (−7.22,−5.33)
16	8.33	0.33	1324	11.9 (10.2,14.7)	3 (2,6)	6 (4,10)	−6.27 (−7.28,−5.52)
32	16.7	0.66	1379	25.7 (21.1,31.3)	5 (3,8)	14 (9,24)	−6.63 (−7.51,−5.95)
64	33.3	1.32	962	53.9 (43.8,67.1)	8 (4,13)	42.0 (27.0,70.8)	−7.36 (−8.24,−6.65)

Note. Region properties for NGC 3351 associations using both *NUV*- and *V*-band tracer stars. [columns 1–3] FWHM of the scale level. [column 4] number of identified associations. [column 5] median, first, and third quartiles for the association radii. [column 6] median number of included tracer stars. [column 7] median number of included DOLPHOT sources. [column 8] median absolute *V*-band magnitude of the associations determined from DOLPHOT photometry

at larger scale levels. By the 64-pc level, the regional photometry is ∼11-per cent different from the PSF photometry.

Since the DOLPHOT photometry is PSF fitted and represents the total flux for that object, it does not require an aperture correction or local background subtraction which can be difficult in crowded environments. There is no aperture correction for the irregular shapes of the stellar associations used in the regional photometry. The regional photometry of the smaller regions at 8 and 16 pc are therefore most impacted by loss of flux due to small apertures. We will therefore use the PSF photometry in our analysis for the rest of the paper.

4.2 SED fitting

To estimate ages, masses, and reddenings of the stellar associations, the CIGALE SED fitting package (Boquien et al. 2019) is used with five-band *NUV, U, V, B, I* photometry of the regions as described in the previous section. Augmentations to CIGALE have been made to enable fitting of single-aged stellar populations as described in Turner et al. (2021). Here, all of the results presented are based on the best-fitting SED corresponding to the minimum reduced chi-squared value, and we do not introduce additional weighting with priors on the age or mass distributions. The fitting is based on the single-aged population synthesis models of Bruzual & Charlot (2003), assuming solar metallicity and a Chabrier (2003) initial mass function (IMF; with standard mass limits of 0.1–100 $M_{\odot}$), and no addition of nebular emission. The Cardelli, Clayton & Mathis (1989) extinction curve with $R_V = 3.1$ is used and a maximum $E(B-V) = 1.5$ is imposed. A more detailed description of the assumptions in the modelling can be found in Turner et al. (2021).

5 RESULTS: STELLAR ASSOCIATION PROPERTIES

Now that we have developed a process for characterizing stellar associations, let us examine the resulting ensemble properties of these structures in NGC 3351 and NGC 1566. We begin by describing the properties of the associations based upon the *NUV* tracer stars, at all four scale levels studied (8, 16, 32, and 64 pc). We discuss both observed and physical properties of these structures. We then discuss differences in the samples of selected structures when the *V*-band tracer stars are used instead. The statistics for the sizes, number of regions, and number of point sources contained in the regions at each scale level are tabulated in Tables 3 and 4. Similar tables for the estimated ages, masses, and extinctions for stellar associations at each scale level are given in Tables 5 and 6.

5.1 Number of regions identified and their sizes

The different scale levels used in our watershed procedure trace the hierarchical structure of star formation from the more compact associations at 8 and 16 pc, to the larger scale stellar associations at 32 and 64 pc. We find that our process identifies of the order of a few hundred up to over 3000 associations depending on the galaxy and scale level (Tables 3 and 4). For NGC 1566 we find around two times more regions than NGC 3351 at each scale level. This potentially follows from the higher SFR values quoted by Leroy et al. (2021) (see Table 1) for NGC 1566. For each galaxy, as the smallest scale level traces the densest peaks of the stellar hierarchy, it also has the fewest regions, while the number of regions is highest at the 32-pc level. As can be seen in Figs 3 and 4, while smaller 8- and 16-pc regions generally lie within the larger 32-pc structures, not every 32-pc region will have substructure at smaller scales. This is due to the requirement that at least two tracer stars be within a region so some of the 32-pc regions are too diffuse to have substructure at the smaller scales. The *V*-band selected tracer stars also result in more detected associations at each scale level with ∼1.5–2 times the number of associations detected with *V*-band tracer stars than are detected with *NUV*-band tracer stars. We will return to examine the possible causes of these differences in Section 5.6.

Each scale level is optimized to identify associations of different sizes. Here, we use the region's effective radius as a measure of the size, where the effective radius is the radius of a circle with an area equal to that of the association. The histograms of the effective radii for each scale are shown in Fig. 6. The sizes peak near the defining Gaussian FWHM used to create the tracer star density maps for each scale level (8, 16, 32, and 64 pc) and are approximately lognormal as shown by the fitted lognormal distributions in black. The high-pass filtering described in Section 3.2 results in distributions that are fairly distinct with overlap only in the wings of the distribution. For example, the *NUV*-band 16-pc scale level sample of stellar associations for NGC 3351 has a median size of 12.4 pc with quartiles of 10 and 15 pc. The distribution also exhibits a tail that extends up to 35 pc. The next scale level at 32 pc has a median size of 26 pc with quartiles of 22–32 pc. While this overlaps the small tail from the previous scale level, the peaks of the distributions are distinct and shows that our method is performing as intended.

Table 4. NGC 1566 region properties.

NGC 1566 *NUV*-band tracer stars							
Scale level			nRegions	Radius	nTracer	nDOLPHOT	M_V (mag)
(pc)	(pix)	(arcsec)		med (.25Q,.75Q) (pc)	med (.25Q,.75Q)	med (.25Q,.75Q)	med (.25Q,.75Q)
16.0	4.63	0.183	983	12.9 (10.9,15.5)	5.0 (3.0,7.0)	5.0 (3.5,8.0)	−8.08 (−8.85,−7.33)
32.0	9.26	0.367	1655	29.3 (24.4,35.7)	6.0 (4.0,11.0)	14.0 (9.0,22.0)	−8.45 (−9.32,−7.7)
64.0	18.5	0.733	1175	57.4 (46.5,72.0)	8.0 (4.0,16.0)	34.0 (20.0,60.0)	−8.92 (−9.84,−8.13)
NGC 1566 *V*-band tracer stars							
16.0	4.63	0.183	2155	12.2 (10.1,15.0)	4.0 (3.0,7.0)	5.0 (3.0,8.0)	−7.59 (−8.36,−6.86)
32.0	9.26	0.367	3150	27.3 (23.0,33.7)	6.0 (3.0,10.0)	11.0 (7.0,19.0)	−8.01 (−8.81,−7.24)
64.0	18.5	0.733	1995	55.4 (45.2,69.3)	8.0 (4.0,17.0)	29.0 (16.0,51.0)	−8.57 (−9.48,−7.66)

Note. Region properties for NGC 1566 associations using both *NUV*- and *V*-band tracer stars. [columns 1–3] FWHM of the scale level. [column 4] number of identified associations. [column 5] median, first, and third quartiles for the association radii. [column 6] median number of included tracer stars. [column 7] median number of included DOLPHOT sources. [column 8] median absolute *V*-band magnitude of the associations determined from DOLPHOT photometry

Table 5. NGC 3351 CIGALE derived properties.

NUV-band CIGALE properties			
Scale level	Age	Mass	$E(B-V)$
(parsec)	$\log_{10}$(yr)	$\log_{10}(M_\odot)$	
	med (.25Q,.75Q)	med (.25Q,.75Q)	med (.25Q,.75Q)
8 pc	6.6 (6.48,6.7)	3.07 (2.62,3.72)	0.155 (0.08,0.25)
16 pc	6.6 (6.48,6.78)	3.15 (2.72,3.64)	0.18 (0.08,0.28)
32 pc	6.7 (6.48,6.9)	3.33 (2.9,3.74)	0.18 (0.06,0.3)
64 pc	6.9 (6.6,7.0)	3.57 (3.24,3.97)	0.14 (0.06,0.26)
V-band CIGALE properties			
8 pc	6.7 (6.6,7.69)	3.13 (2.7,3.6)	0.18 (0.07,0.31)
16 pc	6.7 (6.6,7.26)	3.17 (2.73,3.59)	0.2 (0.08,0.32)
32 pc	6.85 (6.6,7.28)	3.33 (2.92,3.71)	0.21 (0.09,0.33)
64 pc	6.9 (6.85,7.28)	3.54 (3.22,3.91)	0.17 (0.08,0.28)

Note. CIGALE derived properties for both the *NUV*- and *V*-band selected associations in NGC 3351: [col2] median ages. [col3] median masses. [col4] median attenuation.

Table 6. NGC 1566 CIGALE derived properties.

NUV-band CIGALE properties			
Scale level	Age	Mass	$E(B-V)$
(parsec)	$\log_{10}$(yr)	$\log_{10}(M_\odot)$	
	med (.25Q,.75Q)	med (.25Q,.75Q)	med (.25Q,.75Q)
16 pc	6.6 (6.48,6.78)	3.62 (3.2,4.02)	0.15 (0.06,0.25)
32 pc	6.7 (6.48,6.85)	3.78 (3.39,4.21)	0.15 (0.06,0.26)
64 pc	6.85 (6.6,6.9)	4.04 (3.62,4.48)	0.14 (0.04,0.25)
V-band CIGALE properties			
16 pc	6.78 (6.6,7.85)	3.75 (3.34,4.11)	0.16 (0.04,0.28)
32 pc	6.85 (6.7,7.76)	3.91 (3.48,4.27)	0.16 (0.05,0.29)
64 pc	6.9 (6.78,7.72)	4.13 (3.72,4.53)	0.13 (0.05,0.26)

Note. CIGALE derived properties for both the *NUV*- and *V*-band selected associations in NGC 1566: [col2] median ages. [col3] median masses. [col4] median attenuation.

5.2 Number of point sources

We can count the number of point sources enclosed in each association. We define the number of stars (point sources) in two ways: the number of stars that meet the selection criteria and are used to define the association (tracer stars), and the total number of DOLPHOT sources enclosed in each association. It is a requirement that each region contains at least two tracer stars in the filtered image, see Section 3.1 for details. For both galaxies, the median number of tracer stars per region ranges from 3 to 8 as the scale level increases from 8 to 64 pc.

For NGC 3351, the median number of DOLPHOT sources contained in the stellar associations vary from 4 sources at the smallest scale level of 8 pc, up to 49 sources at the 64-pc scale level. For NGC 1566, the median number of contained DOLPHOT sources ranges from 5 to 34.

5.3 Colours

Here, we examine the photometric colours of our sample of stellar associations using the UBVI colour–colour diagram. In past works, the *UBVI* colour–colour diagram has been used extensively for comparison of star cluster populations to single-age stellar population (SSP) model tracks (e.g. Chandar et al. 2010; Adamo et al. 2017; Cook et al. 2019; Deger et al. 2022). Determining whether the photometric properties of the structures are consistent with single-age populations in this way provides a sanity-check on the validity of our watershed method for selecting stellar associations, and on whether to proceed with SED fitting with SSP models. We also compare to composite stellar populations (CSPs) that are formed from exponentially declining SFR, SFR(t) $\sim$ exp($-$ t/τ), with both τ of 2 and 4 Myr.

In Figs 7 and 8, we show the UBVI colour–colour diagrams for associations in NGC 3351 and NGC 1566. For NGC 3351, we plot the stellar associations selected at each of the four scale levels, while for NGC 1566, stellar associations selected at the 8-pc scale level are omitted due to the greater distance of the galaxy. The figures include two columns for each galaxy, one for the NUV-selected associations and a second for the *V*-band associations. In each panel, we overplot an SSP model track with solar metallicty and an escape fraction of zero ($f_{\rm cov}$ = 0) from BC03 in red. The CSP tracks with τ of 2 and 4 Myr in yellow and blue are overplotted on the larger scale levels from 16 to 64 pc.

Overall, the colours do tend to fall along the SSP model track. At the smaller scale levels (8 and 16 pc), there is scatter to the left of the SSP model track into the region of the colour–colour diagram occupied by individual stars. This scatter is due to the low luminosities of the regions and indicates that they would be better modelled by a stellar track than a full stellar population. Scatter to the right of the SSP model track has been shown to be the result of stochastic sampling of the initial mass function for low mass stellar populations (e.g. Fouesneau et al. 2012; Hannon et al. 2019; Whitmore et al. 2020). A single bright red star in a stellar association can pull the colour of that region redward away from the SSP track.

The locus of stellar associations near the beginning of the stellar tracks lies slightly to the right of the SSP track for both galaxies at all scale levels and is consistent with what has been seen previously in

Table 7. NGC 3351 comparison of young (<10 Myr) associations.

Scale level (parsec)	nRegions	nOverlap	Region overlap per cent-Band	Region overlap per cent-Total
8 pc NUV	294	221	75 per cent	46 per cent
8 pc *V* band	403	221	55 per cent	46 per cent
16 pc NUV	704	586	83 per cent	53 per cent
16 pc *V* band	986	587	60 per cent	53 per cent
32 pc NUV	716	590	82 per cent	53 per cent
32 pc *V* band	987	592	60 per cent	53 per cent
64 pc NUV	500	427	85 per cent	59 per cent
64 pc *V* band	642	425	66 per cent	59 per cent

Note. The comparison of overlap between *NUV*- and *V*-band selected young (<10 Myr) associations: [col2] number of regions, [col3] number of regions that have overlap with the other selection band, [col4] per cent of the regions in that selection band that overlap with the other selection, [col5] per cent of all *NUV*- and *V*-band regions that overlap in that selection band.

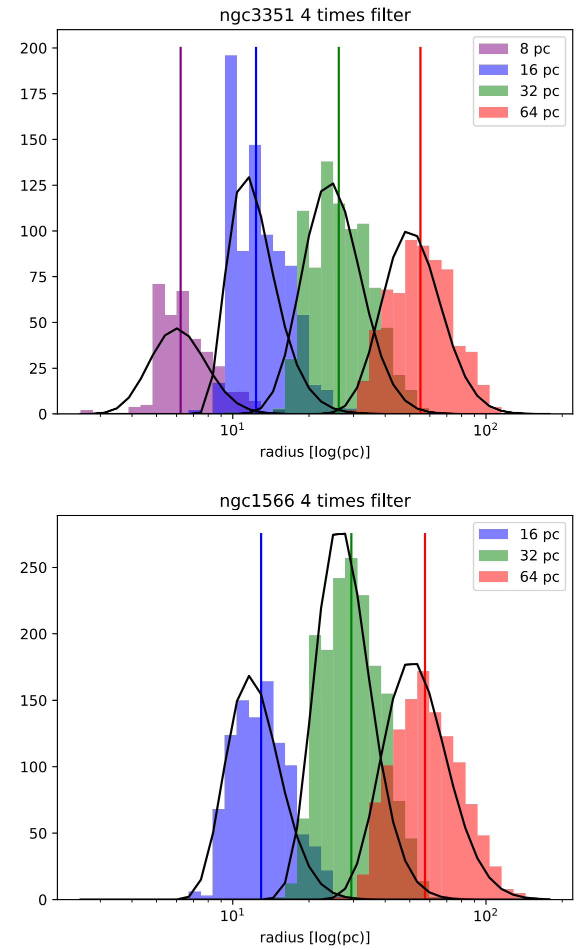

Figure 6. Distribution of effective radii for *NUV* identified stellar associations in NGC 3351 and NGC 1566. A lognormal fitted to each distribution is overplotted in black and the median radius is marked with a vertical line. The median values are also reported in Tables 3 and 4.

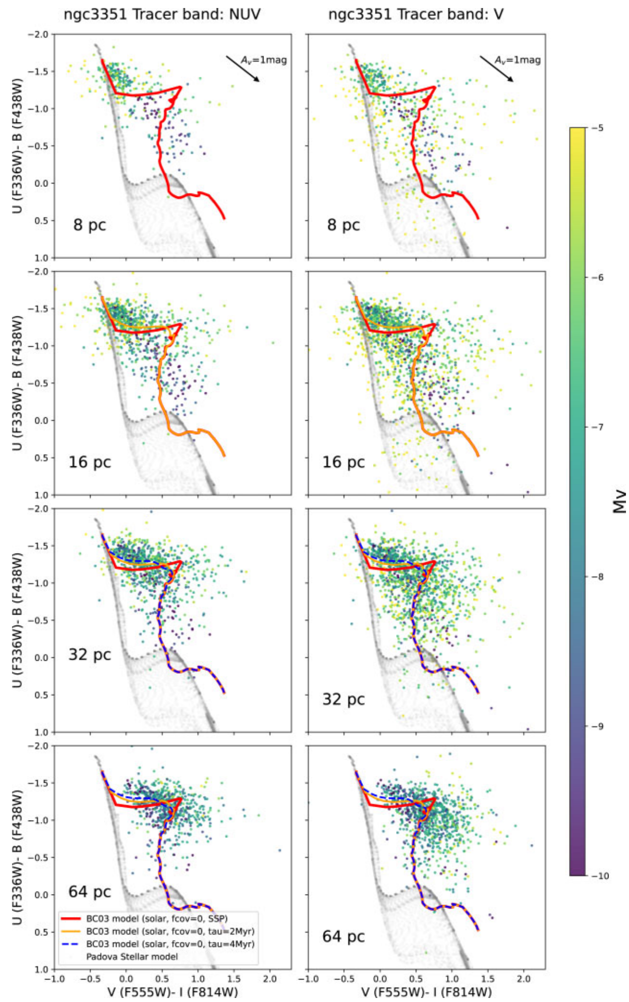

Figure 7. Left: NGC 3351 UBVI colour–colour diagrams for stellar associations selected in the *NUV*-band (left) and *V*-band (right) for four scale levels (8, 16, 32, and 64 pc). The associations are coloured according to their absolute *V*-band magnitude (M_V). The Padova stellar models are shown as grey points and the solar metallicity, $f_{cov} = 0$ evolutionary tracks of synthetic stellar populations from BC03 are overplotted on the associations. The red line traces the path of a single-aged stellar population, while the yellow and blue lines trace composite stellar populations with $\tau = 2$ and $\tau = 4$, respectively.

cluster studies (Chandar et al. 2010). This mismatch from the models is thought to be due to the inability of the models to reproduce the correct colour at the youngest (<3 Myr) ages. Contributions from composite stellar population to the associations could partly explain the shift of the associations at young ages. However, it is difficult

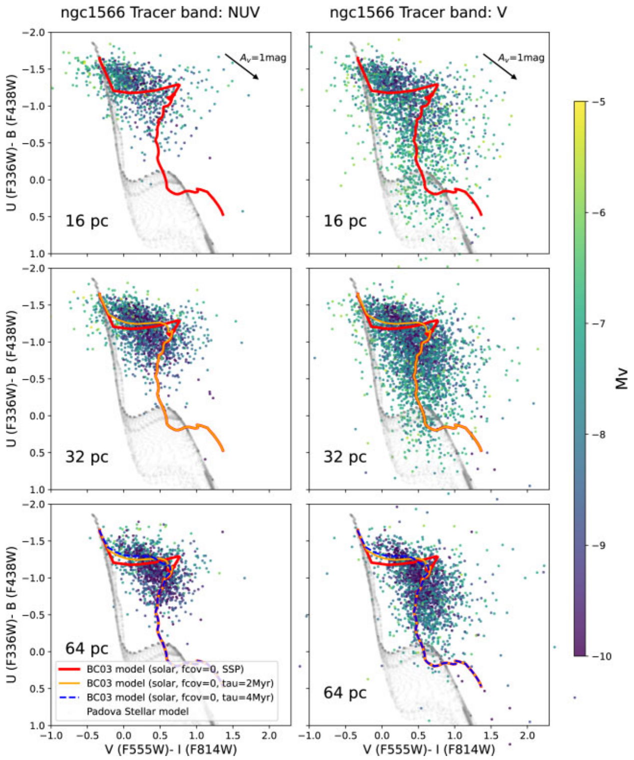

Figure 8. Same as Fig. 7, but for NGC 1566.

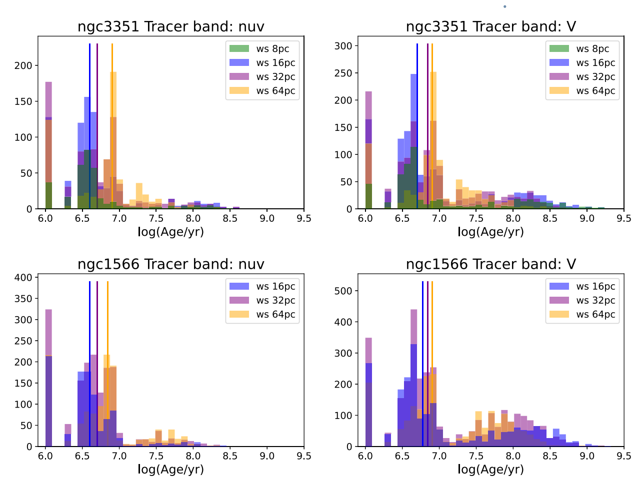

Figure 9. Estimated ages for NGC 3351 (top) and NGC 1566 (bottom) using both the *NUV*- and *V*-band traced watershed associations (8 pc in green, 16 pc in blue, 32 pc in purple, and 64 pc in orange).

to disentangle potential dust effects that could also account for the reddening colours Deger et al. (2022).

We find that for both galaxies, the stellar associations selected at larger scale levels (32–64 pc) have less scatter, as can be expected since larger regions tend to contain more mass overall and stochastic sampling has less of an impact on the resulting observed properties. The loci are tightest at the 64-pc scale and shift redward compared to the smaller scale levels.

It is possible that an SSP is not the best estimate for the larger scale level associations. It would be difficult to randomly coordinate a single burst of star formation over a 32 or 64-pc region and we could expect the larger scale levels to deviate from a pure SSP track. However, the SSP and CSP tracks only deviate slightly in the first 10 Myr of star formation and a simple variation of an exponential star formation history is not enough to explain the observed difference from the 16 to 64-pc scale levels. The redward shift at the 64-pc scale level could be the result of older stellar populations being captured at a higher relative rate as the aperture size increases. A quantitative analysis of the increase in median age of associations with increasing scale level is provided in the next section based upon ages computed from SSP SED fitting. Since the change in the stellar tracks from SSP to CSP is small and fails to explain the shifts in the colour distribution from the 16 to 64-pc scale levels, for the rest of the paper we focus our analysis on the BC03 SSP track. Further study of more complex star formation histories will need to be done in the future.

We also compare the resulting associations at each scale level selected by the different tracer bands. The *NUV*-band selected stellar associations consistently have a tighter, bluer distributions of colours. The *V*-band selected associations have a similar locus at blue colours but also extend to redder colours. This extension to redder colours generally follows along the BC03 SSP track and is apparent at all scale levels for both galaxies.

5.4 Ages and masses

We compute the ages and masses of our stellar associations using the SED fitting code CIGALE with five-band *NUV, U, B, V, I* photometry as input (Section 4). For both galaxies, we find that the distributions of the ages shifts to older values at larger scale levels as can be seen in Fig. 9. This is also reflected in the shift in the loci to redder values at larger scale levels in the colour–colour diagrams, see Figs 7 and 8 as discussed above. As the stellar associations increase in size with larger scale levels, the median ages increase from ∼6.6 to 6.9 log(age/yr) from the 16-pc to the 64-pc scale level for both NGC 3351 and NGC 1566.

Since we are always considering the total flux within a region, including any smaller compact associations, the larger associations could be dominated by light from smaller embedded ones. As the average age of the stellar associations increases at larger scale levels, this shows that the light outside the compact associations does contribute to the overall properties of the larger associations. In future work, it would be interesting to investigate the properties of the larger structures minus the included compact associations to see if we are tracing different star formation populations.

The distribution of ages in Fig. 9 appears to be somewhat bimodal, especially for NGC 1566, with peaks around log(age/yr) = 6.7 and 8.0. Part of this effect is due to a well known (e.g. Chandar et al. 2010) artefact that produces a gap between log(age/yr) = 7.0 and 7.5. This effect is caused by the shape of the BC03 synthetic stellar population tracks, which have sharp bends and loops in this age range (see Fig. 7), effectively shadowing certain ages and shuffling the estimates ages to younger or older ages. Another effect that may artificially overpopulate the diagram with older objects is the inclusion of some fraction of class 1 clusters, since the dolphot program occasionally breaks single, slightly extended objects into two or more separate sources, which are subsequently included as potential associations. This primarily affects the 16-pc scale associations, since the 64-pc associations generally have much larger numbers of tracer stars, hence diluting the inclusion of just a few objects from older clusters. This probably explains the trend toward younger ages (i.e. log(age/yr) ∼7.5–8.0 instead to 8.0–9.0) for the scale 64-pc objects.

The *V*-band selection results in samples of stellar associations that have ∼0.15 dex older median age for 8–32 pc scale levels. While the median of the age distribution for the *V*-band selection is similar

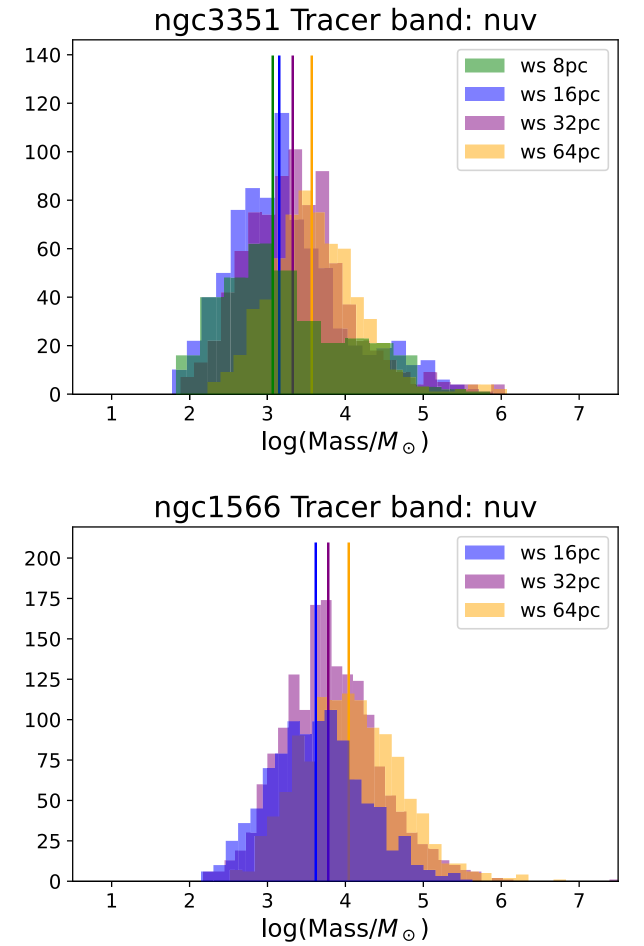

Figure 10. Estimated masses for NGC 3351 (top) and NGC 1566 (bottom) using *NUV*-band traced watershed associations (8 pc in green, 16 pc in blue, 32 pc in purple, and 64 pc in orange).

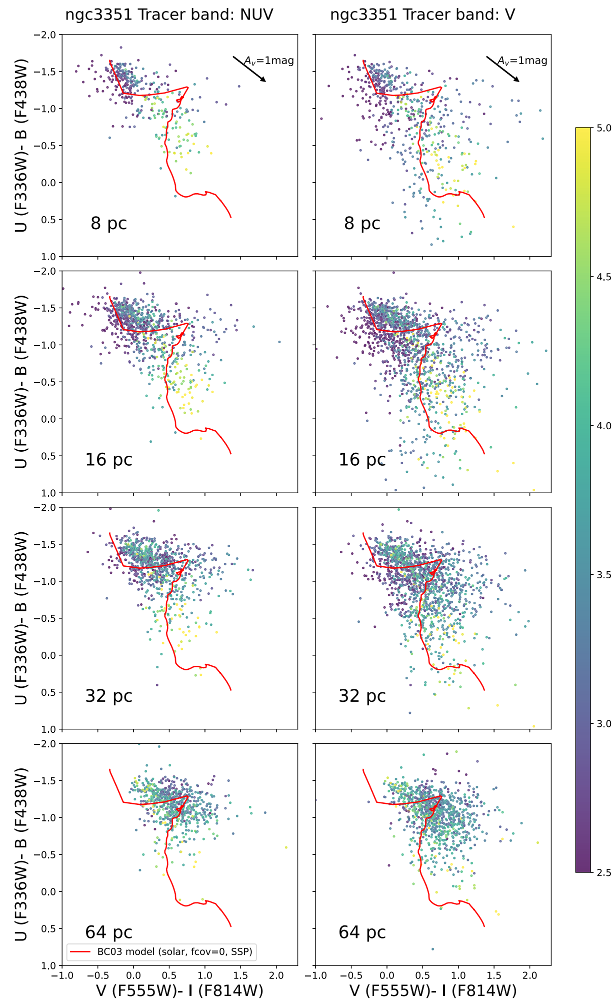

Figure 11. The NGC 3351 regions are colour-coded by their mass. The masses of the watershed regions are estimated using chi-squared fitting to the SED. The left-hand column shows the results of watershed regions created using the *NUV*-band (*F275W*) for the tracer stars. The right-hand column contains results of watershed regions created using the *V*-band (*F555W*) for the tracer stars.

to the *NUV*-band selection, the *V*-band selection finds a larger tail of older/aged associations for both galaxies with log(age/yr) ranging from 7.25 to 9.0 (see Fig. 9). The 64-pc scale level averages over the extremes of the smaller scales and has a tighter distribution of ages that is similar for both *NUV*- and *V*-band selections.

For larger associations, a larger number of DOLPHOT sources are included in each region as previously discussed. Naturally, as the scale level increases, the median mass of the associations also increases (see Fig. 10). The masses of our structures range from $\log(M_\odot) = 3$–7, and the median mass for associations increases by 1.6 times from the 16-pc to the 64-pc scale level for both galaxies.

At each scale level, the masses of the *NUV*-band selected stellar associations in NGC 1566 are on average 2.9 times higher and the *V*-band selected are on average 3.8 times higher than those in NGC 3351. The median masses for NGC 3351 are relatively unchanged regardless of whether the associations are *NUV* or *V*-band selected. The NGC 1566 *V*-band selected associations are about 1.3 times more massive than those selected with *NUV*. However, NGC 1566 is about twice as distant as NGC 3351. The tracer star determination is distance dependent since there is a signal-to-noise cut-off resulting in different absolute magnitude limits resulting in the absolute magnitude of the tracer stars in NGC 1566 being ∼1.5 times larger than those of NGC 3351. We therefore investigate how a different absolute magnitude limits affect the results in Section 5.5.

Figs 11 and 12 show colour–colour diagrams for both NGC 3351 and NGC 1566 which are similar to the ones shown previously but now coloured by the regions' masses. Here, we see that the regions that deviate the most from the SSP track are below $\log(M_\star) \sim 4.5$. This is consistent with the regions which have the lowest mass also having the least number of DOLPHOT sources and therefore are more susceptible to stochastic sampling. The most massive regions $\log(M_\star) > 4.5$ tend to follow the SSP track.

5.5 Dependence on absolute magnitude limit of tracer stars

The multiple physical scale levels of the hierarchy already facilitate the comparison between galaxies at different distances. However, one bias introduced by the difference in distance is that the signal-to-noise cuts placed on the tracer stars resulted in different absolute magnitude limits for NGC 1566 and NGC 3351. We compare the results of selection when a brighter absolute magnitude limit is imposed on the tracer stars for NGC 3351, to enable a fairer comparison to the samples of associations identified in NGC 1566, as the galaxy is more distant and the photometric limit is correspondingly brighter.

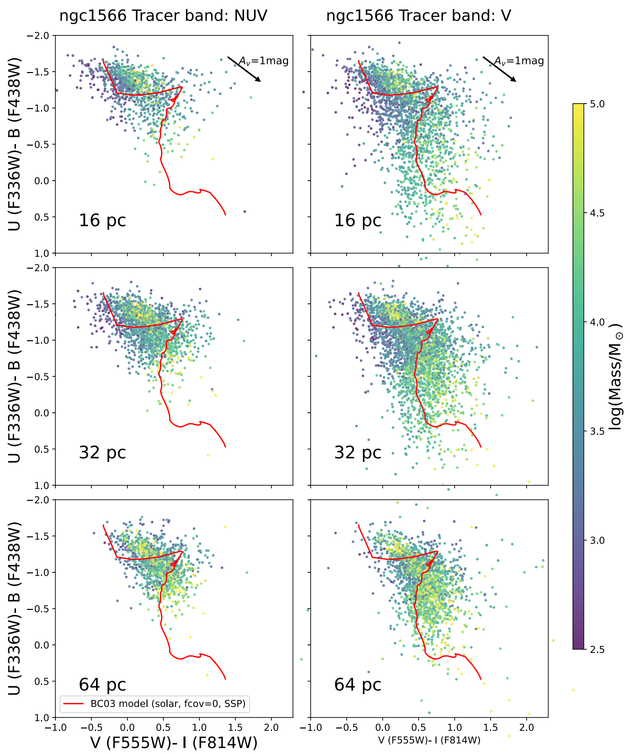

Figure 12. The NGC 1566 regions are colour-coded by their mass. The masses of the watershed regions are estimated using chi-squared fitting to the SED. The left-hand column shows the results of watershed regions created using the *NUV*-band (*F275W*) for the tracer stars. The right-hand column contains results of watershed regions created using the *V*-band (*F555W*) for the tracer stars.

We perform the watershed analysis for NGC 3351 with brighter limits of $M_{\rm V} < -4.2$ and $M_{\rm NUV} < -6.3$. We find that the number of detected associations ∼2.4 times less with brighter magnitude limits. While the average size and age of the associations remains approximately the same with the magnitude limits applied, the average mass increases slightly at all scale levels. The average $\log\,(M/{\rm M}_{\odot})$ increases slightly by ∼0.25 dex at 16 pc, ∼0.20 dex at 32 pc, and ∼0.15 dex at 64 pc for both the *NUV*- and *V*-band selections. This means that the magnitude limit is systematically cutting small or faint associations that therefore have lower mass even though the size and age distribution remain relatively unchanged. Even with this increase in mass taken into account, NGC 1566 stellar associations still have significantly higher median masses.

5.6 Comparison for selection of young stellar associations

We have tested our method using both *NUV* and *V* band to select tracer stars. The *V*-band selection allows for a fair comparison to the compact cluster catalogues which use the *V* band for cluster detection, while the *NUV*-band selection is done to ensure the inclusion of young associations. The *V*-band tracer stars can be both young and old which allows us to trace stellar associations with a wider range of ages, as shown in Section 5.4. However, it also allows for the possibility of associations defined by chance superpositions of tracer stars from different generations of star formation. The *NUV*-band provides a cleaner selection of young tracer stars and a coeval selection for associations since the emission of bright O and B stars peaks in the UV and have ages of only a few Myr. We now directly compare the overlap between young (<10 Myr) associations found by both bands, see Table 7 for details.

The differences between the young *NUV*- and *V*-band selection are apparent across all smoothing scales. For NGC 3351, there are 294 *NUV*-band associations with estimated ages less than 10 Myr and 403 *V*-band associations at the smallest smoothing scale of 8 pc. 75 per cent of the young *NUV*-band 8-pc associations have overlap with the young *V*-band associations. For the *V*-band selection, 55 per cent of the young associations overlap with the *NUV*-band associations. The amount of associations with overlap between the *NUV*- and *V*-band detection only increases slightly with the larger scale levels. At the largest scale level of 64 pc, the percentage of *NUV*-band regions that are also detected in *V*-band increases to 85 per cent while the percentage of *V*-band regions that overlap with *NUV*-band detections increases to 66 per cent. While there are associations with estimated ages <10 Myr in both *NUV* band and *V* band that are unique, the *V* band detects more associations overall and more young associations with 85–90 per cent of all regions are detected in the *V* band.

Of the young *NUV*-band associations, 2–8 per cent are contained within larger and older *V*-band associations, with the overlap increasing at larger scale levels. For young *V*-band associations, 0.02–5 per cent are contained within an older *NUV*-band association. This means that the determined ages of overlapping associations tend to be in agreement regardless of the selection used.

One possibility for the detection of unique associations in the *V* band is extinction. If the association lies in a dusty region of the galaxy, it may still be visible in the *V* band while it is obscured to below the detection threshold in the *NUV* band. The unique *V*-band regions have on average a slightly higher attenuation with $E(B-V) = 0.28$ mag versus the average of $E(B-V) = 0.195$ mag for the associations that overlap with *NUV* and $E(B-V) = 0.145$ mag for the unique *NUV*-band associations.

Another possibility for the larger number of detected young associations with *V* band is that these could be the result of chance superpositions and not a young association of coeval stars. To test this, we looked at the distribution of both the unique and common associations on a colour–colour diagram. As has be seen in the previous section and in Fig. 11, the *V*-band selection has more associations that lie off to the right of the SSP track. Associations that contain a mix of stellar population ages will scatter off to the right of the SSP track. While most of the *V*-band association still lie near the SSP track, the majority of the associations with large scatter in the *V* band are unique to the *V* band.

Therefore, the *NUV* band can provide a cleaner selection of young coeval stellar associations; however, the detection of these associations is limited by attenuation. The *V*-band selection will allow for detection of associations with a wider ranges of ages and is less affected by dust. Therefore, both selections are useful depending on the science goal. We will use and compare the results from both selections in future papers.

6 RESULTS: COMPARISON TO OTHER DATA SETS

6.1 Comparison to LEGUS star clusters and associations

We compare the previously found LEGUS Class 1, 2, and 3 objects in our two test galaxies to our watershed-defined stellar associations. LEGUS Class 1 and 2 are compact single-peaked clusters while LEGUS Class 3 are multipeaked objects with asymmetric profiles. The

Table 8. NGC 3351.

NGC 3351: *NUV*-band regions compared to LEGUS objects					
Scale level (parsec)	(pix)	(arcsec)	Class 1 number (per cent)	Class 2 number (per cent)	Class 3 number (per cent)
8.0	4.16	0.165	8, 6.78 per cent	22, 27.5 per cent	33, 35.1 per cent
16.0	8.33	0.33	23, 19.5 per cent	56, 70 per cent	78, 83 per cent
32.0	16.7	0.66	35, 29.7 per cent	64, 80 per cent	87, 92.6 per cent
64.0	33.3	1.32	45, 38.1 per cent	68, 85 per cent	90, 95.7 per cent
V-band regions compared to LEGUS objects					
8.0	4.16	0.165	17, 14.4 per cent	29, 36.2 per cent	41, 43.6 per cent
16.0	8.33	0.33	45, 38.1 per cent	63, 78.8 per cent	87, 92.6 per cent
32.0	16.7	0.66	61, 51.7 per cent	72, 90 per cent	91, 96.8 per cent
64.0	33.3	1.32	65, 55.1 per cent	75, 93.8 per cent	93, 98.9 per cent

Note. The number and percentage of LEGUS Class 1 (column 4), Class 2 (column 5), and Class 3 (column 6) objects contained in *NUV* or *V*-band selected associations for NGC 3351.

LEGUS Class 3 are most likely compact associations of stars with projected sizes of a few tens of parsecs and are bright concentrations of star formation in larger stellar associations (Adamo et al. 2017). Our regions from the 16-pc scale level are therefore closest in size to the LEGUS definition of Class 3 while our larger scale levels of 32 and 64 pc trace the larger structure of the surrounding stellar associations. Since LEGUS uses the *V* band for cluster identification, our *V*-band selected associations provide the closest comparison to their cluster studies.

For NGC 3351 at the 16-pc smoothing level, we find 1401 *V*-band associations while LEGUS found a total of 118 Class 1, 80 Class 2, and 94 Class 3 objects. For NGC 1566 at the 16-pc scale level, we find 2230 *V*-band associations while LEGUS found a total of 307 Class 1, 271 Class 2, and 469 Class 3 objects. The LEGUS cluster classification is well defined and optimized to find the compact Class 1 and 2 clusters using concentration indices. The LEGUS Class 3 objects are identified by visual inspection of the cluster candidates as regions that are multipeaked and not compact. The watershed technique adopted in this paper is designed to find regions of multipeaked star formation at distinct scale levels. If all *V*-band associations at the 16-pc scale level are considered compact associations, we find 15 times the number of LEGUS Class 3 for NGC 3351 and 4.8 times the number of LEGUS Class 3 for NGC 1566 when using the watershed technique.

We find that the majority of LEGUS-defined Class 3 objects are contained within our associations starting at the 16-pc scale level. The statistics for the number and percentage of Class 1, 2, and 3 LEGUS objects that are contained within both the *NUV*- and *V*-band traced associations are outlined in Table 8 for NGC 3351 and Table 9 for NGC 1566. While the watershed technique is not optimized to identify compact clusters, Class 1 and 2 compact clusters may still lie within larger associations. If the compact clusters get broken into multiple tracer stars by DOLPHOT, they may be identified at the 8 or 16-pc scale level. However, if the compact clusters are identified by only a single DOLPHOT source, they would not be included unless they are part of a larger association.

The watershed technique is designed to find stellar associations. For NGC 3351, the 16-pc *V*-band associations contain only 36 per cent of the Class 1 compact clusters but include 93 per cent of the LEGUS Class 3 compact associations. The 32 and 64-pc smoothing levels contain, respectively, 97 per cent and 99 per cent of the Class 3 compact associations. For NGC 1566, the 16-pc *V*-band associations contain 28 per cent of the Class 1 clusters and 68 per cent of the LEGUS Class 3 compact associations. The percentage of LEGUS Class 3 compact associations increases to 95 per cent and 94 per cent at the 32 and 64-pc smoothing levels. The watershed-defined associations are finding the majority of the LEGUS Class 3 compact associations. Fig. 13 shows the UBVI colour–colour diagrams for the *V*-band stellar associations (in blue) as well as the LEGUS Class 3 compact associations at the 16-pc scale level. The LEGUS Class 3 compact associations that are found within the watershed stellar associations are shown in orange while the LEGUS Class 3 objects not contained within the associations are black squares.

Fig. 14 compares the chi-squared estimated ages, masses, and extinctions of 16-pc *V*-band associations for NGC 3351 (top) and NGC 1566 (bottom) to the LEGUS Class 1, 2, and 3 objects. For NGC 1566, the median masses for the LEGUS objects are less than that of the 16-pc regions. The lower masses for the LEGUS clusters could be due to their compact sizes. For NGC 3351, the median ages of both the Class 2 and 3 objects are similar to the median ages of the watershed associations while the Class 1 compact clusters have an older median log(age/yr) of ∼1.5 dex. For NGC 1566, the median ages of all LEGUS objects are higher than the *V*-band watershed associations. The LEGUS Class 3 compact associations are also selecting an older population than the watershed associations which could be why there is, on average, less overlap for the LEGUS objects and watershed associations for NGC 1566 than there is for NGC 3351.

6.2 Comparison to H II region population

We compare the spacial distribution of stellar associations to H α images from the PHANGS–H α survey (Razza et al., in preparation) as an independent check on our association definition and age estimates. Our watershed process was designed to find young stellar associations. By checking against the distribution of H α emission, we can determine if our algorithm is indeed recovering young stars that are physically associated and thus properly age-dated.

The *V*-band tracer stars select associations with a wider range of ages than the *NUV* band (see Section 5). We therefore compare the H α emission to age-binned stellar association regions created using the *V*-band tracer stars to see the distribution of both young and old associations.

Figs 15 and 16 show that the youngest stellar associations with ages of 1 to 3 Myr (shown as blue regions) trace the H α emission in both NGC 3351 and NGC 1566. Stellar associations with slightly older ages of 3–5 Myr (shown in green) are already less tightly associated with the H α emission. The oldest stellar associations traced by the *V*-band light with ages greater than 60 Myr (shown as the red contours)

Table 9. NGC 1566.

NGC 1566: *NUV*-band regions compared to LEGUS clusers					
Scale level			Class 1	Class 2	Class 3
(parsec)	(pix)	(arcsec)	number (per cent)	number (per cent)	number (per cent)
16.0	4.63	0.183	21, 6.84 per cent	86, 31.7 per cent	234, 49.9 per cent
32.0	9.26	0.367	59, 19.2 per cent	167, 61.6 per cent	381, 81.2 per cent
64.0	18.5	0.733	78, 25.4 per cent	181, 66.8 per cent	390, 83.2 per cent
V-band regions compared to LEGUS objects					
16.0	4.63	0.183	86, 28 per cent	150, 55.4 per cent	320, 68.2 per cent
32.0	9.26	0.367	160, 52.1 per cent	234, 86.3 per cent	442, 94.2 per cent
64.0	18.5	0.733	179, 58.3 per cent	229, 84.5 per cent	442, 94.2 per cent

Note. The number and percentage of LEGUS Class 1 (column 4), Class 2 (column 5), and Class 3 (column 6) objects contained in *NUV* or *V*-band selected associations for NGC 1566.

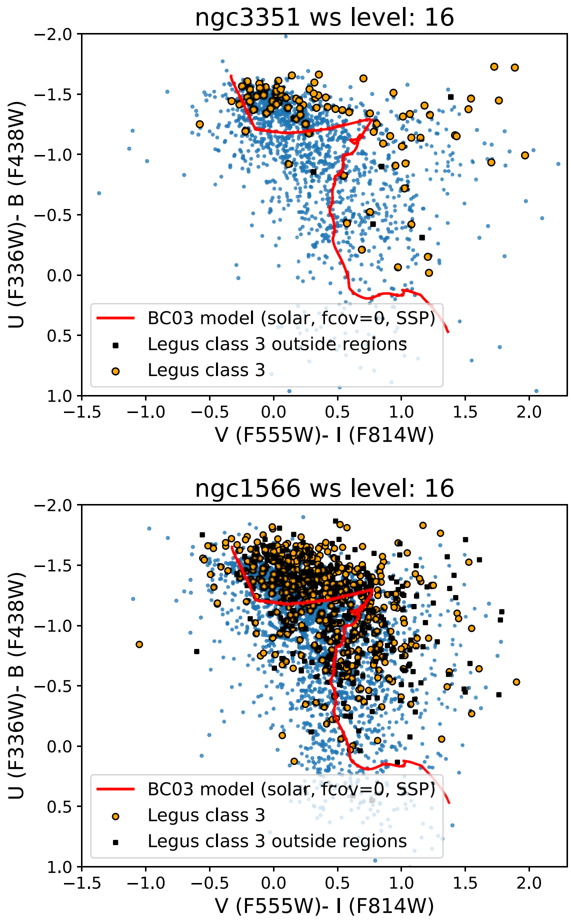

Figure 13. *UBVI* colour–colour diagrams for the *V*-band stellar associations (in blue) as well as the LEGUS Class 3 compact associations at the 16-pc scale level. The majority of the LEGUS Class 3 compact associations lie within our defined *V*-band regions (shown in orange circles) for NGC 3351 *(top)* and NGC 1566 *(bottom)*. The LEGUS Class 3 compact associations that lie outside of the defined regions (black squares) tend to be older or scattered redward of the BC03 SSP track.

are completely uncorrelated with the brightest H *α* light. Since only the youngest (1–3 Myr) associations trace the H *α* light, which is only produced by young stars, this is a good independent check that our stellar associations are indeed tracing the young starlight. Future papers by the PHANGS team, including Scheuermann et al. (2023), perform a detailed analysis of the correlation between stellar associations and a catalogue of H *α*-identified H II regions recently developed (Kreckel et al. 2019; Santoro et al. 2022).

6.3 Comparison to molecular cloud population

Using the stellar association catalogues described above, we take an initial look at their correlation with molecular clouds detected in the PHANGS–ALMA CO(2–1) data. While such analysis will be extensively developed in forthcoming papers, as it is central to main science goals of PHANGS to map the evolution of multiscale structure to deduce star formation time-scales and efficiencies and investigate molecular cloud life cycle (Grasha et al. 2018; Kruijssen et al. 2018, 2019; Schinnerer et al. 2019; Chevance et al. 2020; Kim et al. 2021, 2022; Pan et al. 2022), we provide and initial analysis here. We examine the extent of pixel overlap between PHANGS–ALMA CO(2–1) molecular cloud catalogues (Rosolowsky et al. 2021; Hughes et al., in preparation) and stellar association regions. We use the molecular cloud catalogues developed by the PHANGS project using PYCPROPS, an updated version of the CPROPS algorithm (Rosolowsky & Leroy 2006), described in detail in Rosolowsky et al. (2021).

PYCPROPS segments the CO emission into molecular clouds using a seeded watershed algorithm. The algorithm first identifies local maxima from the CO data. Maxima must have a brightness that is as least twice as bright as the local 'merge level', the emission level that contains at least one neighbour. The minimum number of pixels required to be uniquely associated with the maxima is determined by the beam size of the data and equal to number of pixels included in 25 per cent of the solid angle of the beam ($N > 0.25\Omega_{\rm bm}/\Omega_{\rm pix}$). The identified local maxima are then used to seed the watershed algorithm which segments the CO emission into individual clouds.

Since the *HST* data have no velocity information, we use a velocity-collapsed CPROPS map. When multiple CO clouds are detected along the same line of sight, we compare with the most massive cloud detected along the line of sight. Full details on the construction of the CPROPS molecular cloud catalogues and associated maps are given in Rosolowsky et al. (2021).

Figs 17 and 18 show the velocity-collapsed CPROPS map, in grey-scale, with the 64-pc *NUV*-selected scale level stellar associations overplotted in orange. For our initial comparison, we use the *NUV*-selected associations since (i) we are not interested in the older associations found with the *V*-band and (ii) to ensure a more coeval selection of stellar associations. For NGC 3351, the ALMA field is fully covered by PHANGS–HST. For NGC 1566, the PHANGS–HST data cover the majority of the ALMA map, but does not fully

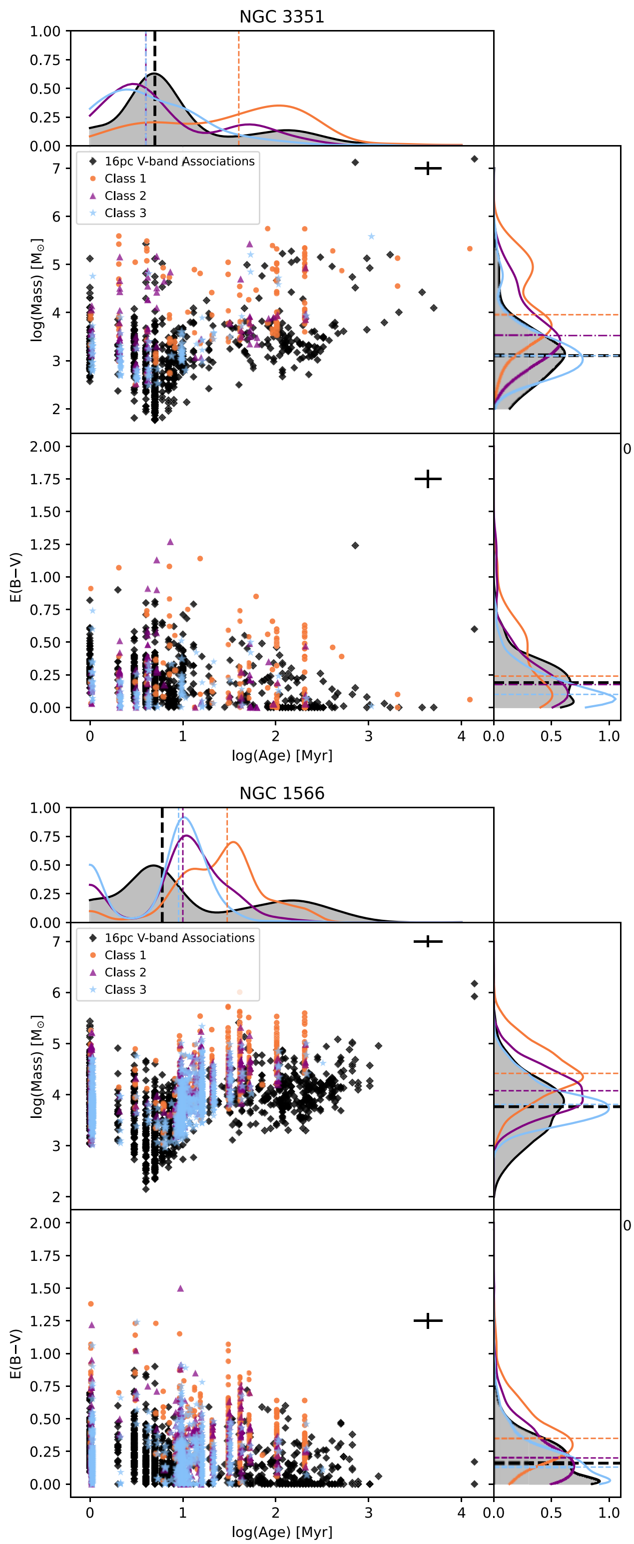

Figure 14. Comparison for NGC 3351 *(top)* and NGC 1566 *(bottom)* of the 16-pc *V*-band watershed associations (black diamonds) chi-squared estimated ages, masses, and $E(B-V)$ to LEGUS objects Class 1 (blue stars), Class 2 (purple triangles), and Class 3 (orange circles). The top histogram in each figure shows the distributions of ages for the 16-pc watershed associations and LEGUS objects while the side histograms show the distribution of the masses and $E(B-V)$.

extend to the edges. For consistency, we will only consider regions with both ALMA and *HST* coverage.

We calculate the per cent overlap between the stellar association regions and the velocity-collapsed CPROPS map. We find the per cent area of overlapping CPROPS and NUV-selected stellar association regions by doing a pixel-by-pixel comparison of the maps. We also calculate the percentage of stellar association regions that overlap with CPROPS clouds at every stellar association scale level.

The ALMA beam size for NGC 3351 is 71 pc while the beam for the more distant NGC 1566 is 110 pc. This means that our 64-pc scale level is closest to the beam size of the ALMA data. In the central ring of NGC 3351, the NUV-selected stellar associations trace a star-forming ring that overlaps the CPROPS regions. The broader NUV light mostly avoids the bright ALMA CPROPS regions in the flocculent spiral arms of NGC 3351. When comparing the per cent pixel overlap between the 64-pc scale level and the CPROPS regions, only 15 per cent of the CPROPS area overlaps the NUV-selected stellar associations while 18 per cent of the area covered by the 64-pc scale level associations overlaps with the CPROPS regions as shown in Table 10.

For NGC 1566, the two brightest spiral arms show overlap between NUV-selected star formation and CPROPS regions. Therefore, the percentage of pixel overlap of the stellar associations is higher than seen for NGC 3351 at every scale level with 55 per cent of the 64-pc scale level area overlapping with the CPROPS regions, see Table 10. Even though significantly more of the stellar associations in NGC 1566 overlap with CPROPS clouds than in NGC 3351, the percentage of the CPROPS area that contains 64-pc stellar associations is similarly small at only 12 per cent. This could be due in part to the larger ALMA beam size of 110 pc for NGC 1566.

As the physical scale of the stellar associations increases, the percentage of the total association area coincident with molecular gas decreases, likely because the larger regions include more area that has not participated in recent star formation. Concurrently, the percentage of the total molecular gas overlap increases, but not in a manner that also results in an increase of the total association area that overlaps.

The majority of the CO clouds by number do not have any overlap with the stellar associations with 67–73 per cent of the molecular clouds having no corresponding associations at the smallest common scale level of 16 pc. This decreases to 42 per cent for both galaxies at the largest stellar scale level of 64 pc. This fraction is similar in both galaxies, which is interesting because in NGC 1566 a much larger percentage of the stellar association regions have overlap with CPROPS regions than in NGC 3351. The percentage of 64-pc stellar associations that overlap with the CPROPS regions 67 per cent for NGC 1566 and only 30 per cent for NGC 3351. Therefore, more of the stellar associations are correlated with the molecular clouds in NGC 1566 than in NGC 3351. These fractions can provide a constraint on the time-scales over which clouds appear inactive (Schruba et al. 2010; Kruijssen & Longmore 2014; Kruijssen et al. 2018; Pan et al. 2022).

In future studies, we will also investigate using the ALMA CO data to help constrain the extinction values to remove degeneracies in the age estimates. However, in the densest molecular clouds it may be impossible to detect ongoing embedded star formation with our UV and optical data. Upcoming infrared data from *JWST* surveys will be imperative to complete our view of the star formation life cycle from molecular clouds to fully emerged star clusters and associations.

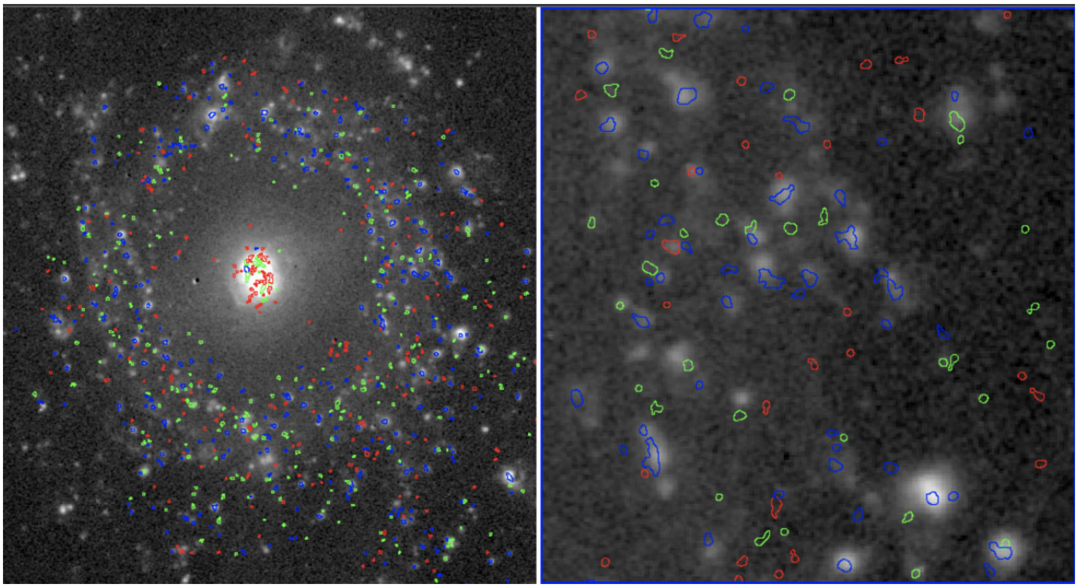

Figure 15. H α image for NGC 3351. Overplotted are the 32-pc regions created using the *V*-band tracer stars in age bins (1–3 Myr in blue, 3–5 Myr in green, and >60 Myr in red).

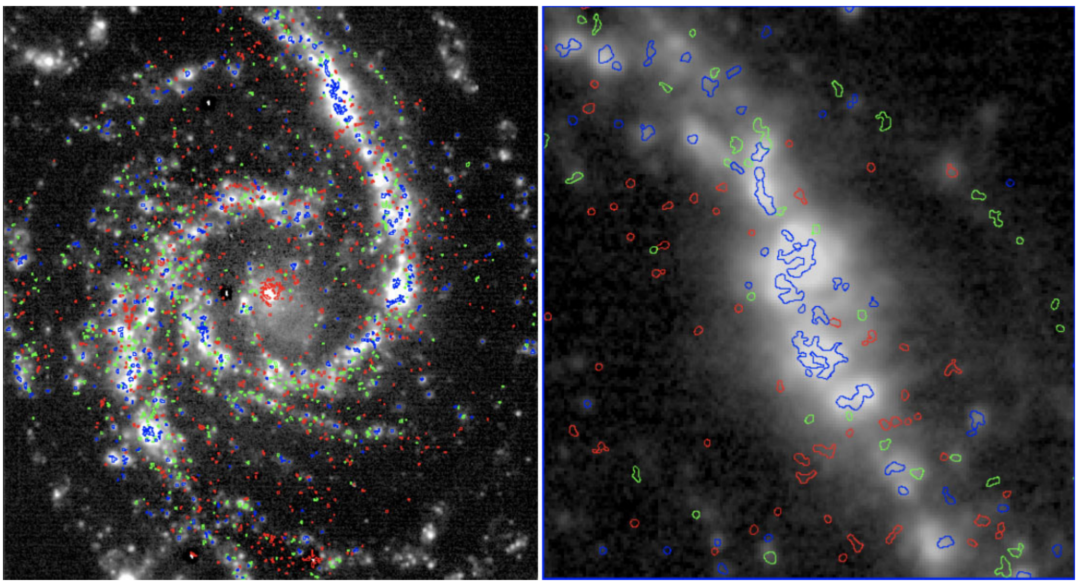

Figure 16. H α image for NGC 1566. Overplotted are the 32-pc regions created using the *V*-band tracer stars in age bins (1–3 Myr in blue, 3–5 Myr in green, and >60 Myr in red).

7 DISCUSSION

Future work is still needed to enable consistent comparison across the entire galaxy sample. PHANGS–ALMA has provided data with matched smoothing scales across the entire sample to allow for consistent comparison of the molecular cloud properties. For the *HST* sample, the galaxies at farther distances, like NGC 1566, will have a higher absolute magnitude limit than nearer galaxies, like NGC 3351. We can make an initial approximation to one of the ways distance affects the consistent detection of associations across the scale levels by testing how the absolute magnitude limit of the tracer stars affects the results. We will look more closely into the potential effects of distance as we seek to do future cross-galaxy correlations.

One advantage to the scale level and watershed hierarchy method we have developed is that it gives consistent physical levels that can be compared directly across a galaxy sample. This allows us to probe the smallest resolvable structures at all distances while still connecting the smaller scale structures to the larger scales probed by more distant galaxies. The multiscale levels also facilitate direct comparison to ancillary data with a variety of resolutions. Since we are already smoothing the tracer star density maps to different physical scale levels for detection, this could potentially eliminate the need to resmooth the initial data to a common resolution and remeasure everything to compare galaxies at different distances like has been necessary for consistency in other studies of both stellar and CO data (Hughes et al. 2013; Larson et al. 2020; Rosolowsky

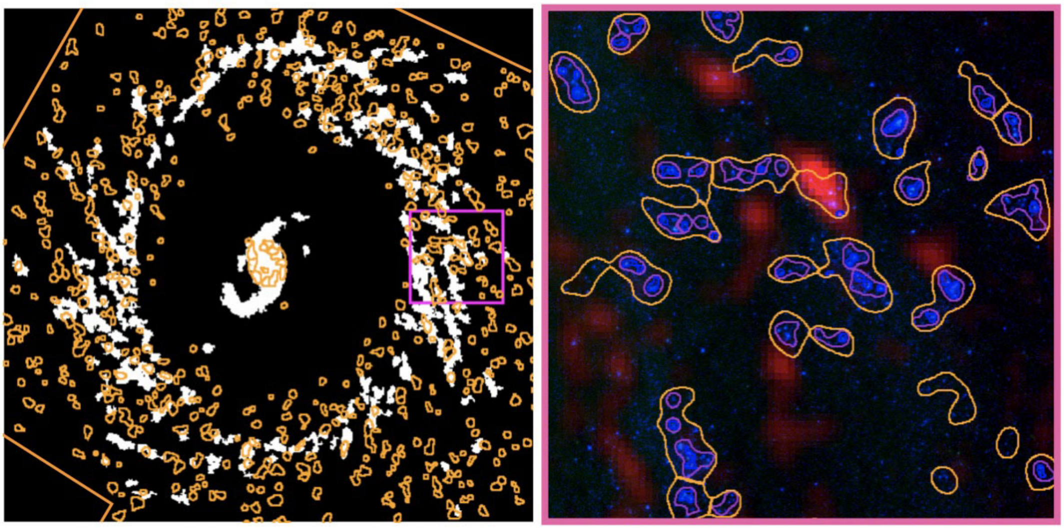

Figure 17. *(Left)* ALMA CPROPS regions for NGC 3351 in white. Overplotted are the 64-pc regions (orange) created using the NUV-tracer stars and a pink box denoting the region of the zoom in panel. The *HST* FOV is larger than the FOV for the ALMA data and is shown as an orange box. *(Right)* Three colour image of the zoom-in panel with ALMA in red, *F275W HST* in blue, and *F555W HST* in green. The corresponding 64-pc (orange), 32-pc (purple), and 16-pc (blue) *NUV*-selected associations are overplotted as regions.

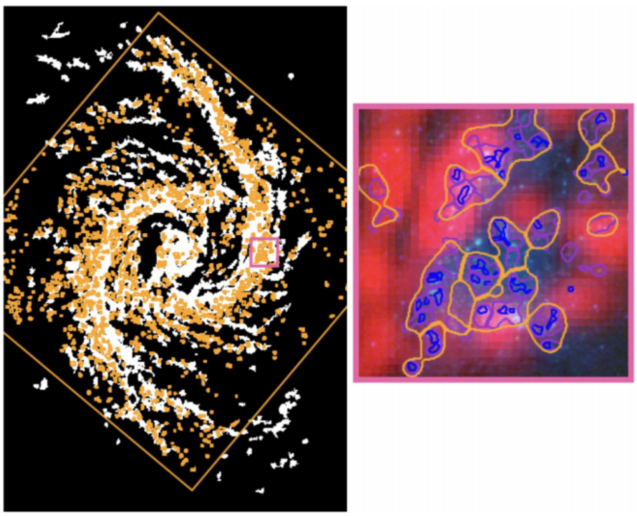

Figure 18. *(Left)* ALMA CPROPS regions for NGC 1566. Overplotted are the 64-pc regions (orange) created using the NUV-tracer stars. The outline of the *HST* footprint is shown as an orange box and the pink box denotes the region of the zoom in panel. *(Right)* Three colour image of the zoom-in panel with Alma in red, *F275W HST* in blue, and *F555W HST* in green. The corresponding 64-pc (orange), 32-pc (purple), and 16-pc (blue) *NUV*-selected associations are overplotted as regions.

et al. 2021). Future work can be done to check this directly with the larger galaxy sample.

8 SUMMARY AND CONCLUSIONS

We present our method of using a watershed algorithm with DOLPHOT tracer stars to trace stellar associations on a range of scales from 8 to 64 pc. We test different parameters for the watershed algorithm including image filtering and using both *NUV*- and *V*-band selected tracer stars. The properties of the resulting associations are characterized, including their sizes, number of tracer stars, and SED-fitted ages, masses, and extinction. We analyse the extent to which these regions resemble single-age stellar populations by comparing their colours to that of BC03 SSP model track. Finally, we perform an initial comparison of the our watershed-defined stellar associations to previously identified LEGUS star clusters, ground-based H α imaging, and PHANGS–ALMA CO cloud catalogues.

(i) We find that our application of the algorithm successfully identifies populations that are well characterized by single-age stellar populations, and occupy loci in the *UBVI* colour–colour diagram consistent with previously published catalogues of compact clusters and associations.

(ii) The median log(age/yr) is the same for both NGC 3351 and NGC 1566 and increases at larger smoothing scales from log(age/yr) = 6.6 to log(age/yr) = 6.9. The *V*-band tracer stars identify not only young associations but also older associations resulting in a median log(age/yr) that is ∼0.15 dex older than the *NUV*-band selection at all scale levels.

(iii) The stellar associations range in mass from $\log(M/\mathrm{M}_{\odot}) = 3$ to $\log(M/\mathrm{M}\odot) = 7$. As the associations increase in size at larger scale levels, the median mass also increases by ∼1.6 times from the 16- to 64-pc scale level for both galaxies. The masses of the stellar associations identified in NGC 1566 are on average 1.9 times more massive than the associations in NGC 3351 at each corresponding scale level.

(iv) We compare the agreement in young (<10 Myr) associations identified with *NUV*- and *V*-band tracer stars in NGC 3351. We find that there is 46–59 per cent overlap in the corresponding young associations from 8 to 64 pc. Since the *V*-band selection identifies more associations at all scale levels, the majority of the unique associations are from the *V*-band selection where 75–85 per cent of the young *NUV*-band selected associations overlap with the larger sample of *V*-band selected associations. Two factors seem to be contributing to the unique detections in *V* band: attenuation and chance superpositions of stars from uncorrelated populations.

Table 10. *HST* NUV stellar association overlap with ALMA CPROPS catalogues.

NGC 3351:				
Scale level (pc)	NUV association per cent pixel overlap	CPROPS per cent pixel overlap	NUV association per cent region overlap	CPROPS per cent region overlap
16	37	2	34	33
32	25	6	29	46
64	18	15	29	58
NGC 1566:				
Scale level (pc)	NUV association per cent pixel overlap	CPROPS per cent pixel overlap	NUV association per cent region overlap	CPROPS per cent region overlap
16	76	1	75	27
32	64	5	69	48
64	55	12	67	58

Therefore, the *NUV*-band selection can provide a cleaner selection of young coeval stellar associations; however, the *V*-band selection is necessary if associations with a wider range of ages are desired.

(v) We compare our overlap of our regions to previously identified LEGUS objects. Most of the LEGUS Class 3 compact associations are contained within the watershed-defined associations by the 16-pc smoothing level with 93 per cent for NGC 3351 and 68 per cent for NGC 1566 of the LEGUS Class 3 objects being contained within the *V*-band watershed associations. The percentage of included LEGUS objects increases at larger smoothing scales. The 16-pc *V*-band watershed associations for NGC 3351 have the same median age as LEGUS Class 2 and Class 3 objects, while the 16-pc *V*-band watershed associations for NGC 1566 are on average younger than all classes of LEGUS objects.

(vi) We compare the spatial distribution of stellar associations to H α emission as an independent check on our association definition and age fitting. We find that the youngest stellar associations with ages between 1 and 3 Myr trace the H α distribution of light. By 3–5 Myr, the stellar associations already start to become less associated with the H α. Older stellar associations with ages greater than 60 Myr are completely unassociated with the H α light.

(vii) We compare the overlap between *NUV*-selected associations and velocity-collapsed CPROPS molecular cloud catalogues. We find that the percentage of CPROPS regions that have overlap with 64-pc stellar associations is $\sim$58 per cent for both galaxies. However, the percentage of 64-pc stellar associations that overlap with the CPROPS regions is only 29 per cent for NGC 3351 and 67 per cent for NGC 1566. Therefore, more of the stellar associations are correlated with the molecular clouds in NGC 1566 than in NGC 3351.

(viii) The correlation between the CPROPS molecular clouds and *NUV* stellar associations varies with environment in the galaxy. In the dense spiral arms of NGC 1566, there are large overlaps between CPROPS regions and stellar associations. In more diffuse CO regions like the inter-arm region of NGC 1566 and disc of NGC 3351, there is less overlap between the CPROPS regions and stellar associations.

The method presented here will be applied to all 38 galaxies in the PHANGS–HST sample. This paper provides a first look at the comparisons that can be performed using our multiscale stellar association catalogues. The stellar associations are vital to studying the stellar life cycle from molecular clouds to emerging stellar complexes.

ACKNOWLEDGEMENTS

This research is based on observations made with the NASA/ESA *Hubble Space Telescope* obtained from the Space Telescope Science Institute, which is operated by the Association of Universities for Research in Astronomy, Inc., under NASA contract NASA5-26555. Support for programme number 15654 was provided through a grant from the STScI under NASA contract NAS5-26555.

This paper makes use of the following ALMA data: ADS/JAO.ALMA#2015.1.00925.S and ADS/JAO.ALMA#2015.1.00956.S. ALMA is a partnership of ESO (representing its member states), NSF (USA), and NINS (Japan), together with NRC (Canada), MOST and ASIAA (Taiwan), and KASI (Republic of Korea), in cooperation with the Republic of Chile. The Joint ALMA Observatory is operated by ESO, AUI/NRAO, and NAOJ.

This research has made use of the NASA/IPAC Extragalactic Database (NED), which is operated by the Jet Propulsion Laboratory, California Institute of Technology, under contract with NASA.

JMDK gratefully acknowledges funding from the Deutsche Forschungsgemeinschaft (DFG) in the form of an Emmy Noether Research Group (grant no. KR4801/1-1), as well as from the European Research Council (ERC) under the European Union's Horizon 2020 research and innovation programme via the ERC Starting Grant MUSTANG (grant agreement no. 714907). COOL Research DAO is a decentralized autonomous organization supporting research in astrophysics aimed at uncovering our cosmic origins.

SD was supported by funding from the European Research Council (ERC) under the European Union's Horizon 2020 research and innovation programme (grant agreement no. 101018897 CosmicExplorer).

KK and EJW gratefully acknowledge funding from DFG in the form of an Emmy Noether Research Group (grant no. KR4598/2-1, PI Kreckel).

TGW acknowledges funding from ERC under the European Union's Horizon 2020 research and innovation programme (grant agreement no. 694343).

RSK acknowledges support from ERC via the Synergy Grant 'ECOGAL' (project ID 855130), from the Heidelberg Cluster of Excellence (EXC 2181-390900948) 'STRUCTURES', funded by the German Excellence Strategy, from DFG in the Collaborative Research Center SFB 881 'The Milky Way System' (funding ID 138713538, subprojects A1, B1, B2, and B8), and from the German Ministry for Economic Affairs and Climate Action in project 'MAINN' (funding ID 50OO2206). RSK also thanks for HPC resources and data storage supported by the Ministry of Science, Research and the Arts of the State of Baden-Württemberg (MWK) and DFG through grants INST 35/1314-1 FUGG and INST 35/1503-1 FUGG, and for computing time from the Leibniz Computing Center (LRZ) in project pr74nu.

KG was supported by the Australian Research Council through the Discovery Early Career Researcher Award (DECRA) Fellowship DE220100766 funded by the Australian Government.

DATA AVAILABILITY

The data underlying this article can be retrieved from the Mikulski Archive for Space Telescopes at https://archive.stsci.edu/hst/search_retrieve.html under proposal GO-15654. High-level science products are provided at https://archive.stsci.edu/hlsp/phangs-hst, including science-ready mosaicked imaging associated with HST GO-15654 with digital object identifier and all multiscale association regions and calculated properties developed in this paper.

REFERENCES

Adamo A., Kruijssen J. M. D., Bastian N., Silva-Villa E., Ryon J., 2015, MNRAS, 452, 246
Adamo A. et al., 2017, ApJ, 841, 131
Adamo A. et al., 2020, MNRAS, 499, 3267
Anand G. S. et al., 2021, MNRAS, 501, 3621
Bastian N., Ercolano B., Gieles M., Rosolowsky E., Scheepmaker R. A., Gutermuth R., Efremov Y., 2007, MNRAS, 379, 1302
Boquien M., Burgarella D., Roehlly Y., Buat V., Ciesla L., Corre D., Inoue A. K., Salas H., 2019, A&A, 622, A103
Bruzual G., Charlot S., 2003, MNRAS, 344, 1000
Calzetti D. et al., 2015, AJ, 149, 51
Cardelli J. A., Clayton G. C., Mathis J. S., 1989, ApJ, 345, 245
Cartwright A., Whitworth A. P., 2004, MNRAS, 348, 589
Chabrier G., 2003, PASP, 115, 763
Chandar R. et al., 2010, ApJ, 719, 966
Chandar R., Fall S. M., Whitmore B. C., Mulia A. J., 2017, ApJ, 849, 128
Chevance M. et al., 2020, MNRAS, 493, 2872
Cook D. O. et al., 2019, MNRAS, 484, 4897
Deger S. et al., 2022, MNRAS, 510, 32
Dolphin A. E., 2002, MNRAS, 332, 91
Elmegreen B. G., 2008, ApJ, 672, 1006
Elmegreen B. G., 2018, ApJ, 853, 88
Emsellem E. et al., 2022, A&A, 659, A191
Fouesneau M., Lançon A., Chandar R., Whitmore B. C., 2012, ApJ, 750, 60
Girardi L., Bertelli G., Bressan A., Chiosi C., Groenewegen M. A. T., Marigo P., Salasnich B., Weiss A., 2002, A&A, 391, 195
Gouliermis D. A., 2018, PASP, 130, 072001
Gouliermis D. A., Schmeja S., Klessen R. S., de Blok W. J. G., Walter F., 2010, ApJ, 725, 1717
Gouliermis D. A. et al., 2015, MNRAS, 452, 3508
Gouliermis D. A. et al., 2017, MNRAS, 468, 509
Grasha K. et al., 2018, MNRAS, 481, 1016
Hannon S. et al., 2019, MNRAS, 490, 4648
Hughes A. et al., 2013, ApJ, 779, 44
Johnson L. C. et al., 2016, ApJ, 827, 33
Kennicutt R. C., Jr, 1998, ARA&A, 36, 189
Kim J. et al., 2021, MNRAS, 504, 487
Kim J. et al., 2022, MNRAS, 516, 3006
Krause M. G. H. et al., 2020, Space Sci. Rev., 216, 64
Kreckel K. et al., 2019, ApJ, 887, 80
Kruijssen J. M. D., 2012, MNRAS, 426, 3008
Kruijssen J. M. D., Longmore S. N., 2014, MNRAS, 439, 3239
Kruijssen J. M. D., Schruba A., Hygate A. E. P. S., Hu C.-Y., Haydon D. T., Longmore S. N., 2018, MNRAS, 479, 1866
Kruijssen J. M. D. et al., 2019, Nature, 569, 519
Krumholz M. R., McKee C. F., Bland -Hawthorn J., 2019, ARA&A, 57, 227
Lada C. J., Lada E. A., 2003, ARA&A, 41, 57
Larson K. L. et al., 2020, ApJ, 888, 92
Lee J. C. et al., 2022, ApJS, 258, 10
Leroy A. K. et al., 2021, ApJS, 257, 43
Marigo P., Girardi L., Bressan A., Groenewegen M. A. T., Silva L., Granato G. L., 2008, A&A, 482, 883
Pan H.-A. et al., 2022, ApJ, 927, 9
Rodríguez M. J., Baume G., Feinstein C., 2019, A&A, 626, A35
Rosolowsky E., Leroy A., 2006, PASP, 118, 590
Rosolowsky E. W., Pineda J. E., Kauffmann J., Goodman A. A., 2008, ApJ, 679, 1338
Rosolowsky E. et al., 2021, MNRAS, 502, 1218
Santoro F. et al., 2022, A&A, 658, A188
Scheuermann F. et al., 2023, MNRAS
Schinnerer E. et al., 2019, Messenger, 177, 36
Schmidt M., 1959, ApJ, 129, 243
Schruba A., Leroy A. K., Walter F., Sand strom K., Rosolowsky E., 2010, ApJ, 722, 1699
Thilker D. A. et al., 2022, MNRAS, 509, 4094
Turner J. A. et al., 2021, MNRAS, 502, 1366
Ward J. L., Kruijssen J. M. D., 2018, MNRAS, 475, 5659
Ward J. L., Kruijssen J. M. D., Rix H.-W., 2020, MNRAS, 495, 663
Wei W. et al., 2020, MNRAS, 493, 3178
Whitmore B. C. et al., 2020, ApJ, 889, 154
Whitmore B. C. et al., 2021, MNRAS, 506, 5294
Wright N. J., 2020, New Astron. Rev., 90, 101549

APPENDIX A: HIGH-PASS FILTERING

We compare the use of two different high-pass filters. We subtract a map that is smoothed to a scale 4 times larger than the original map, and another smoothed to scale that is 8 times larger. To determine which filtering step may be more appropriate for selection of associations, we analyse the distribution of sizes from the resulting regions compared to those in the original unfiltered image. We find that both high-pass filtered images (4 and 8 times larger) have size distributions with median effective radii similar to the FWHM of the Gaussian smoothing kernel (see Table A1). As expected, the filtering does result in fewer regions detected at each scale level compared to when no filtering is applied. Fig. A1 shows that the regions that are being filtered out are at the tails of the size distribution and that we are effectively sampling the bulk of the distribution.The high-pass filtering removes more of the larger sized regions at each scale level. This is desired since the scale levels are defined to

Table A1. NGC 3351 filter step comparison.

Scale level (parsec)	nRegions	radius med (.25Q,.75Q)
NGC 3351, 4 times filter step, NUV tracer stars		
8.0	334	6.23 (5.53,7.66)
16.0	807	12.4 (10.3,15.3)
32.0	838	26.1 (21.6,32.4)
64.0	641	55.2 (45.2,67.4)
NGC 3351, 8 times filter step, NUV tracer stars		
8.0	544	6.59 (5.53,8.32)
16.0	909	13.7 (10.9,17.0)
32.0	883	28.4 (23.1,36.5)
64.0	634	59.6 (47.3,75.4)

Note. Properties of NUV associations with two different high-pass filters: 4 times filter step and 8 times filter step. [col1] scale level. [col2] number of regions [col3] the median, first and third quartile radius of regions.

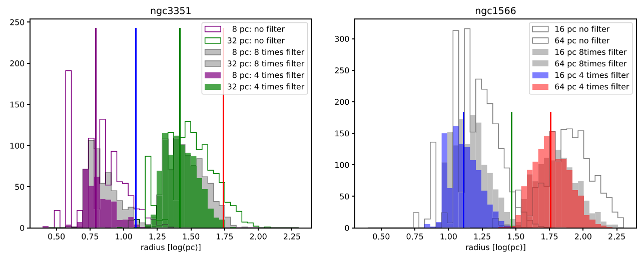

Figure A1. Distribution of region sizes at two smoothing levels for each galaxy. We show how the distribution changes with no filtering applied (empty histogram), and with two different high-pass filtering steps: filter step of 4 times the smoothing level (32–128 pc) shown as the filled coloured histograms and a filter step of 8 times the smoothing level (32–256 pc) shown as the grey filled histograms. Vertical lines make the median size values of the 4 times filtered distributions. Both filtering steps give similar median size values for the regions.The 4 times filtering produces the tightest size distribution with the least overlap between scale levels.

emphasize different sized associations. The larger structures that are filtered out at the small scale levels will be recovered at larger scale levels.

The high-pass filters effectively remove tails in the distribution at both the high and the low end that are present at all scale levels in the original unfiltered image. Both of the high-pass filtered images therefore have a tighter distribution of sizes than the unfiltered image; however, the larger filter step (8 times larger) produces a wider spread of region sizes than the smaller filter step (4 times larger) and produces size distributions with more overlap between the different scale levels as shown in Fig. A1. Since the specific smoothing scales are defined with the purpose of selecting specific sizes of structures and minimizing the overlap between the different scale levels, we adopt the smaller filter step which produces a tighter distribution of region sizes. Therefore, we will use the 4 times high-pass filter as our fiducial choice.

[1] *AURA for the European Space Agency (ESA), Space Telescope Science Institute, 3700 San Martin Drive, Baltimore, MD 21218, USA*
[2] *Caltech/IPAC, California Institute of Technology, 1200 E. California Blvd., Pasadena, CA 91125 USA*
[3] *Gemini Observatory/NSF's NOIRLab, 950 N. Cherry Avenue, Tucson, AZ 85719, USA*
[4] *Department of Physics and Astronomy, The Johns Hopkins University, Baltimore, MD 21218, USA*
[5] *Space Telescope Science Institute, 3700 San Martin Drive, Baltimore, MD 21218, USA*
[6] *The Oskar Klein Centre for Cosmoparticle Physics, Department of Physics, Stockholm University, AlbaNova, SE-106 91 Stockholm, Sweden*
[7] *Department of Physics and Astronomy, University of Wyoming, Laramie, WY 82071, USA*
[8] *Department of Physics and Astronomy, University of Toledo, Toledo, OH 43606, USA*
[9] *Argelander-Institut für Astronomie, Universität Bonn, Auf dem Hügel 71, D-53121 Bonn, Germany*
[10] *Research School of Astronomy and Astrophysics, Australian National University, Weston Creek, ACT 2611, Australia*
[11] *International Centre for Radio Astronomy Research, University of Western Australia, 35 Stirling Highway, Crawley, WA 6009, Australia*
[12] *Max-Planck-Institut für Astronomie, Königstuhl 17, D-69117 Heidelberg, Germany*
[13] *Institut für Theoretische Astrophysik, Zentrum für Astronomie, Universität Heidelberg, Albert-Ueberle-Straße 2, D-69120 Heidelberg, Germany*
[14] *Interdisziplinäres Zentrum für Wissenschaftliches Rechnen, Universität Heidelberg, Im Neuenheimer Feld 205, D-69120 Heidelberg, Germany*
[15] *Astronomisches Rechen-Institut, Zentrum für Astronomie der Universität Heidelberg, Mönchhofstraße 12–14, D-69120 Heidelberg, Germany*
[16] *Cosmic Origins Of Life (COOL) Research DAO, coolresearch.io*
[17] *Department of Astronomy, The Ohio State University, 140 West 18th Avenue, Columbus, OH 43210, USA*
[18] *Department of Physics, University of Alberta, Edmonton, AB T6G 2E1, Canada*
[19] *Max-Planck-Institut für extraterrestrische Physik, Giessenbachstraße 1, D-85748 Garching, Germany*
[20] *Sub-department of Astrophysics, Department of Physics, University of Oxford, Keble Road, Oxford OX1 3RH, UK*

This paper has been typeset from a TEX/LATEX file prepared by the author.